

Article

$\text{Na}_3[\text{Ru}_2(\mu\text{-CO}_3)_4]$ as a Homogeneous Catalyst for Water Oxidation; HCO_3^- as a Co-Catalyst

Shanti Gopal Patra ^{1,2,*} , Totan Mondal ¹ , Krishnamoorthy Sathiyar ¹ , Amir Mizrahi ³, Haya Kornweitz ¹ and Dan Meyerstein ^{1,4,*}

¹ Chemical Sciences Department and The Radical Research Center, Ariel University, Ariel 40700, Israel; totan88@gmail.com (T.M.); krishgprs@gmail.com (K.S.); hayak@ariel.ac.il (H.K.)

² Department of Chemistry, Arunachal University of Studies, NH52, Namsai, Arunachal Pradesh 792103, India

³ Chemistry Department, Nuclear Research Centre Negev, Beer-Sheva 84105, Israel; amirmizrachi@gmail.com

⁴ Chemistry Department, Ben-Gurion University, Beer-Sheva 84190, Israel

* Correspondence: shantigp@ariel.ac.il (S.G.P.); danm@ariel.ac.il (D.M.); Tel.: +972-50-5415982 (D.M.)

Abstract: In neutral medium (pH 7.0) $[\text{Ru}^{\text{III}}\text{Ru}^{\text{II}}(\mu\text{-CO}_3)_4(\text{OH})]^{4-}$ undergoes one electron oxidation to form $[\text{Ru}^{\text{III}}\text{Ru}^{\text{III}}(\mu\text{-CO}_3)_4(\text{OH})_2]^{4-}$ at an $E_{1/2}$ of 0.85 V vs. NHE followed by electro-catalytic water oxidation at a potential ≥ 1.5 V. When the same electrochemical measurements are performed in bicarbonate medium (pH 8.3), the complex first undergoes one electron oxidation at an E_{pa} of 0.86 V to form $[\text{Ru}^{\text{III}}\text{Ru}^{\text{III}}(\mu\text{-CO}_3)_4(\text{OH})_2]^{4-}$. This complex further undergoes two step one electron oxidations to form $\text{Ru}^{\text{IV}}\text{Ru}^{\text{III}}$ and $\text{Ru}^{\text{IV}}\text{Ru}^{\text{IV}}$ species at potentials (E_{pa}) 1.18 and 1.35 V, respectively. The $\text{Ru}^{\text{IV}}\text{Ru}^{\text{III}}$ and $\text{Ru}^{\text{IV}}\text{Ru}^{\text{IV}}$ species in bicarbonate solutions are $[\text{Ru}^{\text{IV}}\text{Ru}^{\text{III}}(\mu\text{-CO}_3)_4(\text{OH})(\text{CO}_3)]^{4-}$ and $[\text{Ru}^{\text{IV}}\text{Ru}^{\text{IV}}(\mu\text{-CO}_3)_4(\text{O})(\text{CO}_3)]^{4-}$ based on density functional theory (DFT) calculations. The formation of HCO_3^- in the course of the oxidation has been demonstrated by DFT. The catalyst acts as homogeneous water oxidation catalyst, and after long term chronoamperometry, the absorption spectra does not change significantly. Each step has been found to follow a proton coupled electron transfer process (PCET) as obtained from the pH dependent studies. The catalytic current is found to follow linear relation with the concentration of the catalyst and bicarbonate. Thus, bicarbonate is involved in the catalytic process that is also evident from the generation of higher oxidation peaks in cyclic voltammetry. The detailed mechanism has been derived by DFT. A catalyst with no organic ligands has the advantage of long-time stability.

Keywords: electrocatalysis; water oxidation; carbonate; peroxomonocarbonate; DFT; ruthenium carbonate



Citation: Patra, S.G.; Mondal, T.; Sathiyar, K.; Mizrahi, A.; Kornweitz, H.; Meyerstein, D. $\text{Na}_3[\text{Ru}_2(\mu\text{-CO}_3)_4]$ as a Homogeneous Catalyst for Water Oxidation; HCO_3^- as a Co-Catalyst. *Catalysts* **2021**, *11*, 281. <https://doi.org/10.3390/catal11020281>

Academic Editors: Vincenzo Baglio, Minhua Shao, Carlo Santoro and David Sebastián

Received: 30 January 2021

Accepted: 18 February 2021

Published: 21 February 2021

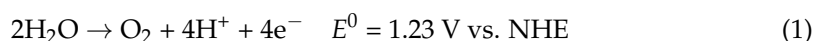
Publisher's Note: MDPI stays neutral with regard to jurisdictional claims in published maps and institutional affiliations.



Copyright: © 2021 by the authors. Licensee MDPI, Basel, Switzerland. This article is an open access article distributed under the terms and conditions of the Creative Commons Attribution (CC BY) license (<https://creativecommons.org/licenses/by/4.0/>).

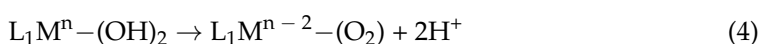
1. Introduction

With the decrease in the abundance of fossil fuels (coal, petroleum, and natural gas), the search for alternative energy sources is an immense challenge for mankind [1]. In the past few decades, solar energy and electricity have been considered as the source of alternative energies [2]. It is important to note that in nature, plants employ the highly sophisticated machinery called Photosystem II to convert sunlight into fuel [3]. It uses the calcium-manganese based oxo-cluster (CaMn_4O_5 core) as the catalyst to split water via a series of proton-coupled electron transfer (PCET) processes [4]. Because of pollution free combustion and high energy density, hydrogen is considered a green and sustainable source of energy that can be produced by splitting water using solar photocatalysis [5] or electrocatalysis [6]. For this, an efficient and durable catalyst is in high demand for promoting proton coupled evolution of oxygen with the removal of four electrons (Equation (1)). However, this process is sluggish and needs electrochemically high overpotential to oxidize the water.



This is due to the complexity of the process: Formation of the O-O bond along with four protons and four electrons, which results in slow kinetics and thermodynamics [7]. RuO₂ and IrO₂ serve as highly efficient heterogeneous water oxidation catalysts [8]. Apart from oxides, sulfide, nitride, and phosphide transition metal compounds have been shown as catalysts of the oxygen evolution reaction, OER [9].

Over the years, extensive research has been carried out for the development of heterogeneous [10] and homogeneous [11] OER catalysts based on earth-abundant low cost materials. In the literature, a plethora of materials based on Mn [12,13], Fe [14,15], Co [15–20], Ni [21,22], and Cu [23], can be found which act as promising water oxidation catalysts. Catalysts involving costly metal, e.g., Ru [24] and Ir [25], are also reported. In the past few decades, enormous efforts have been put forward for the ruthenium-based molecular water oxidation catalysts [26,27]. Meyer and coworker [28] first reported the polypyridyl ruthenium-based water oxidation catalyst; *cis*, *cis*-[Ru^{II}(bpy)₂(py)(H₂O)]₂O⁴⁺ (where py = pyridine and bpy = bipyridine) widely known as the “blue dimer” (BD). BD has been considered as the landmark in the mechanistic study of water oxidation catalysts (WOC) [29]. It has been proposed and verified by various in situ experimental studies that before OER the catalyst goes through a dimeric oxo species, O=Ru^V-Ru^V=O [30–34]. Three pathways have been proposed for the formation of the O-O bond after the water nucleophilic attack (Equations (3)–(5)) via coupling interaction of two metallo-oxyl/hydroxyl radicals are proposed [31,35].

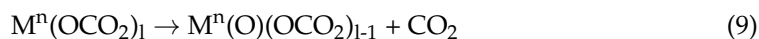
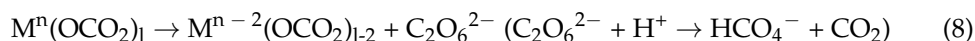
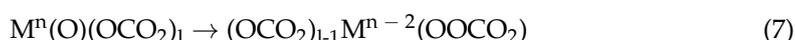
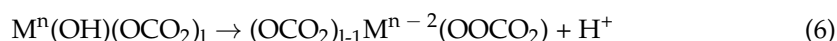


Later on, this mechanism of O-O bond formation became widely accepted by means of many experimental studies on molecular water oxidation catalysts [27,36]. Another important aspect of the BD catalyst in OER is that it involves PCETs [10,37–40]. PCETs are important because of two reasons: (a) Nature employs it in Photosystem II [41] and (b) it can decrease the pK_a of the H₂O molecule bound to the central cation, as a result, the formation of hydroxo/oxo species becomes easier, which stabilizes higher oxidation states (IV, V) [29]. However, in this context, it should be noted that the true role of homogeneous WOCs based on transition metal ions supported by organic/inorganic ligands are in question because in many cases it has been found that those complexes act as precursors for the generation of more reactive nanoparticles on the electrode surface [7].

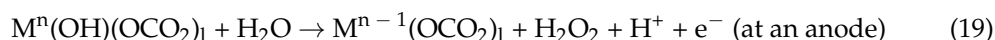
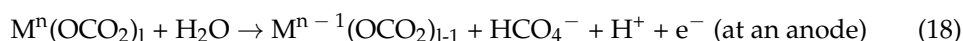
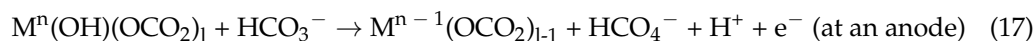
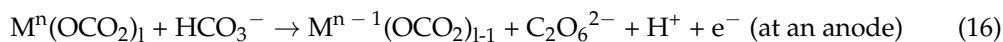
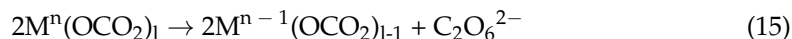
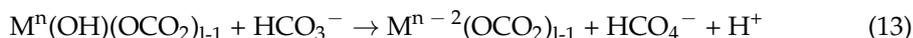
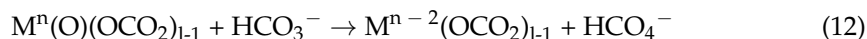
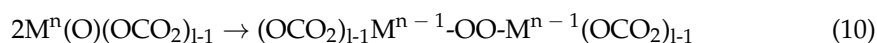
Carbonate/bicarbonate acts as co-catalysts of the water oxidation processes [42,43]. This is due to the oxidation potential of the CO₃^{•-}/CO₃²⁻ (E⁰ = 1.57 V vs. NHE) [44,45] couple that is significantly lower compared to that of OH[•]/H₂O (E⁰ = 2.73 V vs. NHE) or OH[•]/OH⁻ [42]. Bicarbonate/carbonate can facilitate the water oxidation by two ways: Stabilizing the metal ions in high oxidation states due to its strong σ donor character and/or act as pro-oxidant by forming CO₃^{•-} and/or HCO₄⁻/C₂O₆²⁻. For example, the redox potential of Fe^{III/II} [46], Mn^{III/II} [47], and Ce^{IV/III} [48] in concentrated carbonate solutions is shifted cathodically by 1.09, 0.99, and 1.70 V, respectively, compared to that of their aqueous counterpart. Similarly, other lanthanide carbonates, M^{IV}(CO₃)_n (M = Pr, Tb), can be easily prepared by electrolysis of the carbonate solution at 1.4 V [48]. In 1958, Warburg and Krippahl reported that CO₂ acts as stimulator in the light driven water oxidation process in Photosystem II [49]. Later on, it was accepted as the “bicarbonate effect” by means of experimental studies on the role of CO₂/HCO₄⁻ [50].

The first experimental proof of the OER by copper carbonate was reported by Meyer et al. [51]. It showed the dependence of the catalytic current on metal salt concentration as well as on [CO₃²⁻]/[HCO₃⁻], but did not confirm the oxidation state of the active catalyst (Cu^{III} or Cu^{IV}) in the rate determining step. Later, a Density Functional Theory (DFT) study by Cramer et al. [52] showed the possibility of a Cu^{IV} species as the active

intermediate. However, Meyerstein and coworkers [53] have shown that $\text{Cu}^{\text{III}}(\text{CO}_3)_n^{3-2n}$ is the active intermediate in the electrolysis of $\text{Cu}^{\text{II}}(\text{CO}_3)_n^{2-2n}$ solutions using pulse-radiolysis experiments and DFT studies. In a recent paper, the role of carbonate as a “proton shuttle” has been discussed in the electrocatalytic water oxidation by $\text{Cu}(\text{N},\text{N}'\text{-2,6-dimethylphenyl-2,6-pyridinedicarbox-amidate})$, CuL [54] in the presence of carbonate. In another nickel complex, $\text{Ni}^{\text{II}}(1,4,8,11\text{-tetraazacyclotetra-decane})^{2+}$, $\text{Ni}^{\text{II}}\text{L}_1^{2+}$ the involvement of carbonate has been discussed by Burg et al. [22] where the formation of a $\text{Ni}^{\text{IV}}=\text{O}$ active species via cleavage of the C-O bond of the carbonate has been postulated along with many other processes involving $\text{CO}_3^{2-}/\text{HCO}_3^-$. The formation of peroxo-mono-carbonate in the electro-catalytic water oxidation by some aluminum porphyrin complexes has been reported very recently by Kuttassery et al. [55] in the presence of $\text{CO}_3^{2-}/\text{HCO}_3^-$. Several mechanisms for the role of carbonate in these processes can be proposed [22,45,54,56]:



Followed by reactions (6), (9), (10) or (11) [22]:



As discussed above, the ruthenium based WOCs are promising and have interesting mechanisms of OER activity based on mononuclear and binuclear catalysts. The carbonate complex of ruthenium, $\text{Na}_3[\text{Ru}_2(\mu\text{-CO}_3)_4]$, has been reported by Wilkinson and coworkers [57,58] in 1986, and some electro-chemical properties have been studied by Cotton and coworkers [59]. Since water molecules can be coordinated to the two ruthenium central cations, in higher oxidation states, and this complex has reasonable solubility, though, most of the transition metal carbonates have low solubility in water, and in aqueous solution it seemed reasonable to speculate that it would be an ideal catalyst for electrochemical water oxidation. Herein the OER activity of the complex in the presence and absence of bicarbonate/carbonate are reported. Interestingly, in the presence of bicarbonate/carbonate, the catalyst goes through various oxidation states as obtained from cyclic voltammetry.

2. Results

The dimeric complex of ruthenium, $\text{Na}_3[\text{Ru}_2(\mu\text{-CO}_3)_4]$, is obtained as an orange yellow precipitate by reacting $[\text{Ru}_2(\mu\text{-CH}_3\text{COO})_4\text{Cl}]$ with Na_2CO_3 [59]. X-ray crystal structure [59] shows that four carbonates are bridging the two Ru centers to form the dimer, and the free oxygens of the carbonate ligands are bound to the axial position of a Ru atom present in an

another dimer, making a two dimensional coordination polymeric structure (Figure S1). In the solid-state, no water molecule is found to be bound to the axial position of the ruthenium atoms. Thus, it has been considered that in solution the complex exists as $[\text{Ru}_2(\mu\text{-CO}_3)_4]^{3-}$. The Ru_2^{5+} core has metal-metal (d^6-d^5) bonding with an electronic configuration of $\sigma^2\pi^4\delta^2\delta^*\pi^*1$ and bond order of 2.5 [60]. One interesting aspect of this complex is that, with further oxidation of the complex, electrons are being removed from the antibonding orbitals, resulting in an increase in bond order and strength. As a result, the integrity of the dimeric structure remains intact and is not decomposed. Herein two aspects of catalytic water oxidation are discussed: (a) Catalytic water oxidation in neutral medium and (b) catalytic water oxidation in bicarbonate/carbonate media.

2.1. Catalytic Water Oxidation in Neutral Medium

The complex was first dissolved in water in the presence of 0.20 M NaClO_4 at a pH of 7.0 and cyclic voltammetry was performed. The quasi reversible ($\Delta E_p = E_{pa} - E_{pc} = 107$ mV) oxidation has been observed at an $E_{1/2}$ of 0.85 V vs. NHE (Figure 1).

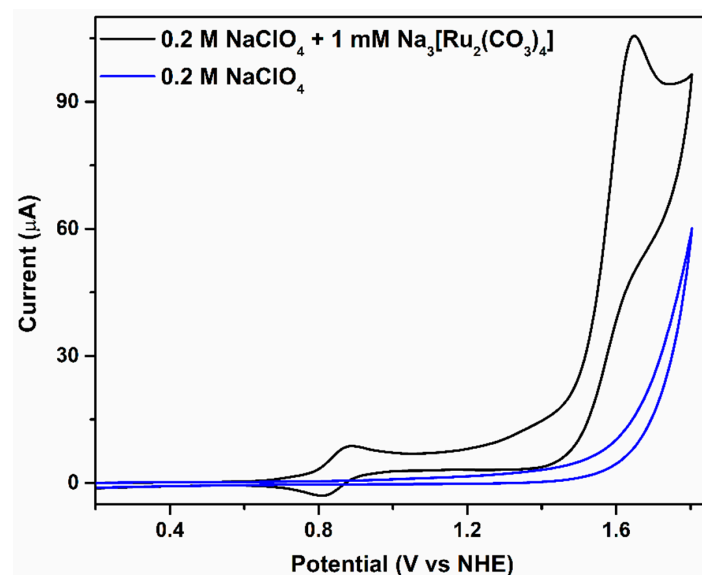


Figure 1. Cyclic voltammograms of a solution containing 0.20 M NaClO_4 (pH 7.0) in the presence and absence of 1.0 mM $\text{Na}_3[\text{Ru}_2(\mu\text{-CO}_3)_4]$ at a scan rate of $50 \text{ mV}\cdot\text{s}^{-1}$ under N_2 atmosphere.

We speculated that in this medium, the high valent site, Ru^{III} , of the complex gets coordinated by OH^- . This fact has also been supported by theoretical calculations that show that when the complex is coordinated by OH^- it gets stabilized by a free energy gain of $-102.32 \text{ kcal}\cdot\text{mol}^{-1}$. The one electron oxidation of the complex from $[\text{Ru}^{\text{II}}\text{Ru}^{\text{III}}(\mu\text{-CO}_3)_4(\text{OH})]^{4-}$ to $[\text{Ru}^{\text{III}}\text{Ru}^{\text{III}}(\mu\text{-CO}_3)_4(\text{OH})_2]^{4-}$ is confirmed by comparing the current with $\text{K}_4[\text{Fe}(\text{CN})_6]$ under similar conditions (Figure S2). In this context, it is important to note that Cotton and coworkers [59] have studied the electrochemical properties of this system and found the same oxidation potential for the $\text{Ru}^{\text{III}}\text{Ru}^{\text{III}}/\text{Ru}^{\text{III}}\text{Ru}^{\text{II}}$ couple. However, herein we show that if we scan the potential further, then a large current can be seen at potentials ≥ 1.5 V vs. NHE. A very weak peak can also be seen at 1.4 V, which indicates the catalytic process goes through high oxidation states of the metal. The first peak is diffusion controlled, as it follows the Randles–Sevcik equation (Equation (20)), i.e., the current is proportional to the square root of the scan rate (Figures 2 and S3).

$$i_d = 0.496n_d \alpha^{1/2} FA[C] \left(\frac{n_d F v D_o}{RT} \right)^{1/2} \quad (20)$$

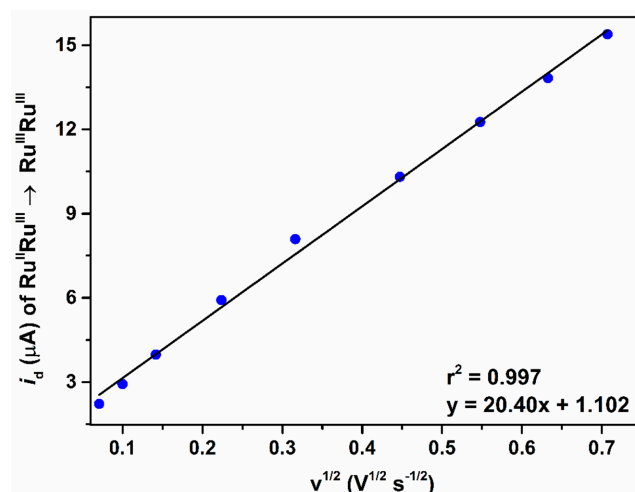


Figure 2. A plot of the anodic peak current (i_d) of the $Ru^{III}Ru^{III}/Ru^{III}Ru^{II}$ peak vs. the square root of the scan rate. The voltammograms are recorded in 1.0 mM $Na_3[Ru_2(\mu-CO_3)_4]$ and 0.20 M $NaClO_4$ (pH 7.0) under N_2 atmosphere.

The diffusion coefficient, D_o , is calculated to be $1.16 \times 10^{-6} \text{ cm}^2 \cdot \text{s}^{-1}$ from the slope of i_d vs. $v^{1/2}$. Using Nicholson's method [61], one calculates the rate constant (k_0) of electron transfer to be $(1.15 \pm 0.15) \times 10^{-3} \text{ cm} \cdot \text{s}^{-1}$ (Table S1). Herein, before water oxidation, the catalyst undergoes oxidation to various other high oxidation states and finally the $O=Ru^{IV}-Ru^{IV}=O$ species is formed (see below), which acts as the active intermediate in the OER. However, other oxidation states can only be seen in cyclic voltammetry with large catalytic currents in the presence of bicarbonate/carbonate.

It is assumed that in the first step in neutral medium $[Ru^{II}Ru^{III}(\mu-CO_3)_4(OH)]^{4-}$ undergoes one electron oxidation and simultaneously coordinates one OH^- to the open axial position of the other Ru^{III} ion to form $[Ru^{III}Ru^{III}(\mu-CO_3)_4(OH)_2]^{4-}$, (Equation (21)).



This is manifested by the pH dependence of the anodic peak potential (E_{pa}). The E_{pa} shifts cathodically with the increase in pH with a slope of $-50 \text{ mV} \cdot \text{pH}^{-1}$ (Figures 3 and S4). The increase in current is due to a contribution from the next step. Further, the water oxidation peak potential also shifts linearly with the pH of the medium (Figures 4 and S5). Thus, protons are involved in the rate determining step of the water oxidation.

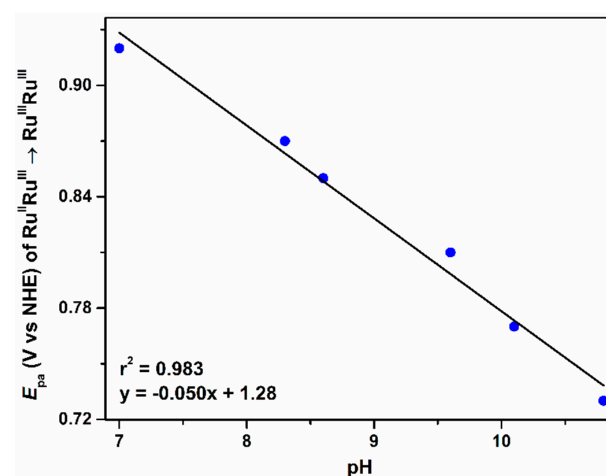


Figure 3. A plot of the anodic peak potential (E_{pa}) of the first redox couple vs. the pH of the medium. The voltammograms are recorded in 1.0 mM $Na_3[Ru_2(\mu-CO_3)_4]$ and 0.20 M $NaClO_4$ aqueous solutions at different pHs with a scan rate of $50 \text{ mV} \cdot \text{s}^{-1}$ under N_2 atmosphere.

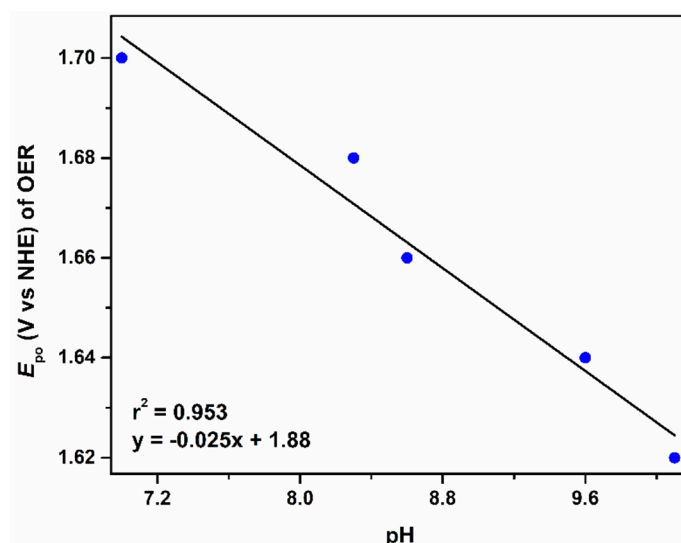


Figure 4. A plot of the water oxidation peak/plateau potential vs. the pH of the medium. The voltammograms are recorded in 1.0 mM $\text{Na}_3[\text{Ru}_2(\mu\text{-CO}_3)_4]$ and 0.20 M NaClO_4 aqueous solutions at different pHs with a scan rate of $50 \text{ mV}\cdot\text{s}^{-1}$ under N_2 atmosphere.

2.2. Catalytic Water Oxidation in Bicarbonate/Carbonate Medium

The complex was dissolved in 0.10 M NaHCO_3 and then cyclic voltammetric measurements were performed at pH 8.3. The cyclic voltammograms of the complex in the presence and absence of NaHCO_3 are compared in Figure 5. Unlike the neutral medium (where only one prominent redox process is observed before the catalytic process), in the presence of bicarbonate, three redox processes before the catalytic water oxidation can be clearly seen. To further study the processes before the catalytic process, a square wave voltammogram was recorded (Figure 6). Interestingly four electrochemical processes are observed: (a) 1st peak due to the redox couple $\text{Ru}^{\text{III}}\text{Ru}^{\text{III}}/\text{Ru}^{\text{III}}\text{Ru}^{\text{II}}$ involving one electron at an E_{pa} of 0.86 V vs. NHE, (b) 2nd peak due to the redox couple $\text{Ru}^{\text{IV}}\text{Ru}^{\text{III}}/\text{Ru}^{\text{III}}\text{Ru}^{\text{III}}$ involving one electron oxidation at 1.18 V, (c) 3rd peak due to the redox couple $\text{Ru}^{\text{IV}}\text{Ru}^{\text{IV}}/\text{Ru}^{\text{IV}}\text{Ru}^{\text{III}}$ involving one electron oxidation at 1.35 V (little bit of large current probably due to a contribution from the next step), and (d) large current due to oxidation of $\text{HCO}_3^-/\text{water}$ at potential ≥ 1.5 V vs. NHE. Next, we shall discuss each step and the mechanisms involved in the process.

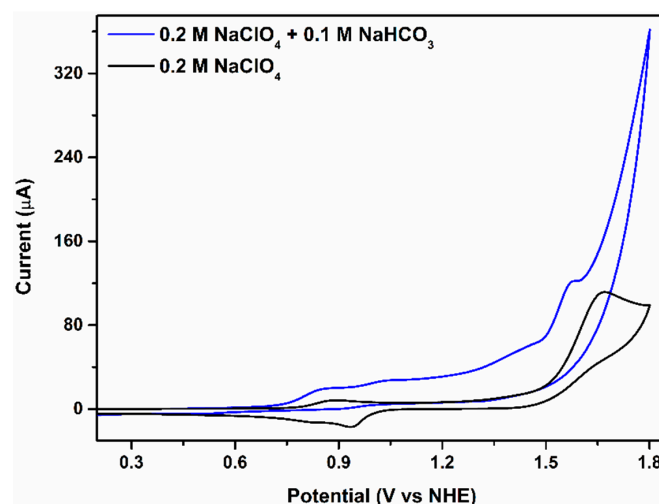


Figure 5. Cyclic voltammograms of a solution containing 1.0 mM $\text{Na}_3[\text{Ru}_2(\mu\text{-CO}_3)_4]$ in the presence of 0.10 M NaHCO_3 (pH 8.3, blue line) and 0.20 M NaClO_4 (pH 7.0, black line) scan rate, 50 mV s^{-1} under N_2 atmosphere.

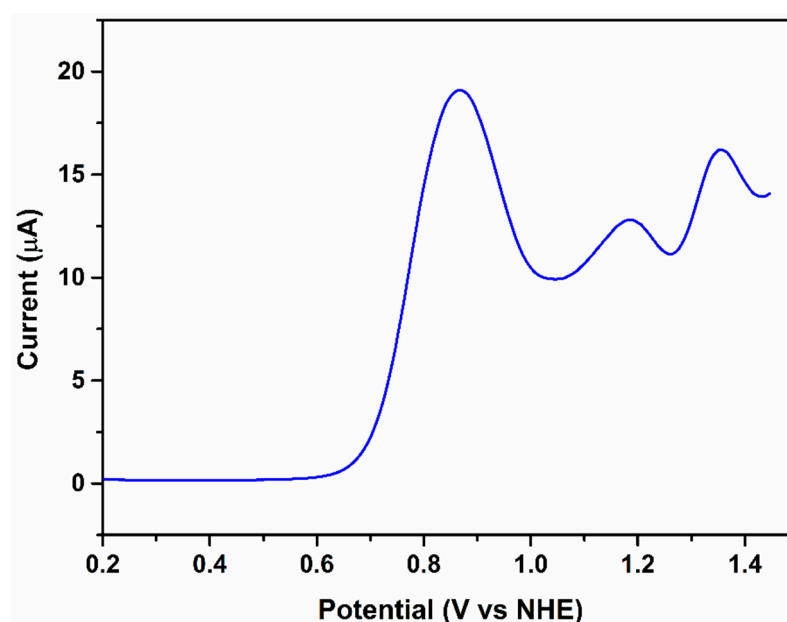


Figure 6. Square wave voltammogram of a solution containing 1.0 mM $\text{Na}_3[\text{Ru}_2(\mu\text{-CO}_3)_4]$ in the presence of 0.10 M NaHCO_3 , pH 8.3, under N_2 atmosphere. Instrumental settings: Amplitude, 0.010 V; frequency, 15.0 Hz.

2.2.1. The First Wave, $\text{Ru}^{\text{III}}\text{Ru}^{\text{III}}/\text{Ru}^{\text{III}}\text{Ru}^{\text{II}}$ Redox Couple

The first quasi-reversible oxidation is observed at 0.86 V and is attributed to the oxidation of $[\text{Ru}^{\text{II}}\text{Ru}^{\text{III}}(\mu\text{-CO}_3)_4(\text{OH})]^{4-}$ to $[\text{Ru}^{\text{III}}\text{Ru}^{\text{III}}(\mu\text{-CO}_3)_4(\text{OH})_2]^{4-}$. In the alkaline medium, the current of the 1st oxidation peak seems to increase, this increase is due to the overlap with the next electrochemical process (Figure S6). The 1st step is a one electron process ($\text{Ru}^{\text{II}}\text{Ru}^{\text{III}} \rightarrow \text{Ru}^{\text{III}}\text{Ru}^{\text{III}}$). It is important to note that in neutral medium, $[\text{Ru}^{\text{II}}\text{Ru}^{\text{III}}(\mu\text{-CO}_3)_4(\text{OH})]^{4-}$ undergoes one electron oxidation to form $[\text{Ru}^{\text{III}}\text{Ru}^{\text{III}}(\mu\text{-CO}_3)_4(\text{OH})_2]^{4-}$ (Equation (21)). The redox potential of the couple, $\text{Ru}^{\text{III}}\text{Ru}^{\text{III}}/\text{Ru}^{\text{III}}\text{Ru}^{\text{II}}$, decreases consistently with increasing pH (Figures 7 and S7).

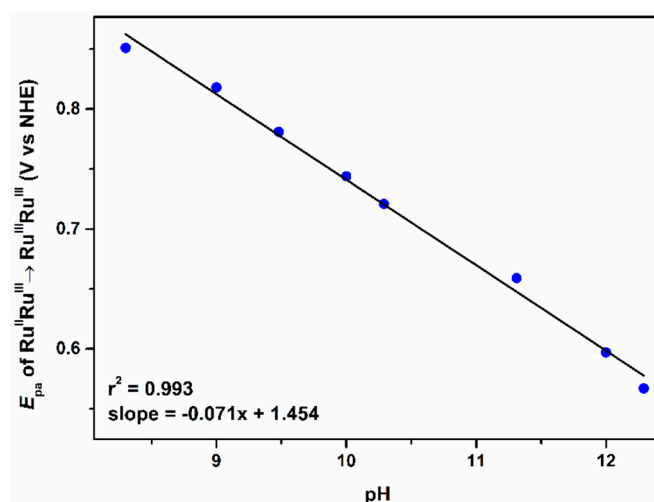


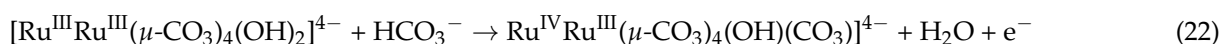
Figure 7. The cyclic voltammograms of the redox wave are recorded in various bicarbonate concentrations. However, no significant change in the peak potential/current was found (Figure S9). This is because bicarbonate replaces the hydroxide ion after the redox process and is not involved in the electron transfer step.

The slope of the plot of E_{pa} of $\text{Ru}^{\text{III}}\text{Ru}^{\text{III}}/\text{Ru}^{\text{III}}\text{Ru}^{\text{II}}$ vs. pH is $-71 \text{ mV}\cdot\text{pH}^{-1}$, which is consistent with Equation (21). It should be noted that the increase in the pH also

increases the ratio $[\text{CO}_3^{2-}]/[\text{HCO}_3^-]$. The scan rate dependence of the first two redox peaks are shown in Figure S8. Diffusion coefficient ($D_0 = 0.51 \times 10^{-6} \text{ cm}^2 \text{ s}^{-1}$) decreases in bicarbonate medium. Further, to check the effect of bicarbonate concentration on the first redox wave, the CVs of the first redox wave were recorded in various bicarbonate concentrations. However, no significant change in the peak potential/current was found (Figure S9). This is because bicarbonate replaces the hydroxide ion after the redox process and is not involved in the electron transfer step.

2.2.2. The Second Wave, $\text{Ru}^{\text{IV}}\text{Ru}^{\text{III}}/\text{Ru}^{\text{III}}\text{Ru}^{\text{III}}$ Redox Couple

The second wave is observed at an $E_{1/2}$ of 0.97 V vs. NHE and is attributed to the oxidation of $[\text{Ru}^{\text{III}}\text{Ru}^{\text{III}}(\mu\text{-CO}_3)_4(\text{OH})_2]^{4-}$ to $[\text{Ru}^{\text{IV}}\text{Ru}^{\text{III}}(\mu\text{-CO}_3)_4(\text{OH})(\text{CO}_3)]^{4-}$ (Equation (22)) with the simultaneous release of one proton, i.e., a PCET process is taking place. The proposal that when the Ru center is oxidized to the +4 oxidation state the axial OH^- is replaced by a carbonate ligand is based on the DFT calculations, see below. The involvement of one electron is based on the comparison of the peak current



with $\text{K}_4[\text{Fe}(\text{CN})_6]$ under identical conditions (Figure S6). The peak current for the second wave is 7.6 μA , which is comparable to the current (7.1 μA) of $\text{Fe}^{\text{III/II}}$ couple in ferrocyanide. The pH dependence (Figure S7) of the peak potential confirms the PCET process. However, the slope of the peak potential (E_{pa}) of the $[\text{Ru}^{\text{IV}}\text{Ru}^{\text{III}}(\mu\text{-CO}_3)_4(\text{OH})(\text{CO}_3)]^{4-}/[\text{Ru}^{\text{III}}\text{Ru}^{\text{III}}(\mu\text{-CO}_3)_4(\text{OH})_2]^{4-}$ is only $-18 \text{ mV}\cdot\text{pH}^{-1}$ (Figure 8) against the theoretical value of $-59 \text{ mV}\cdot\text{pH}^{-1}$. However, the partial overlap with the third electrochemical process (Figure S7), which increases with the pH, might cause this. This peak is quasi-reversible ($\Delta E_{\text{p}} = 124 \text{ mV}$), and the reduction peak can be seen in the reverse scan.

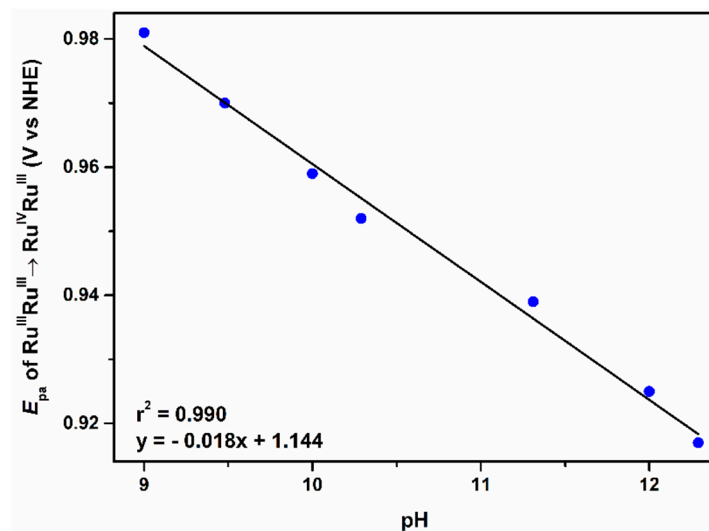
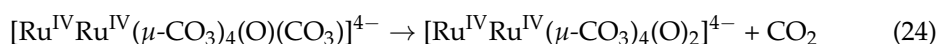


Figure 8. A plot of the anodic peak potential (E_{pa}) of the $\text{Ru}^{\text{IV}}\text{Ru}^{\text{III}}/\text{Ru}^{\text{III}}\text{Ru}^{\text{III}}$ redox couple vs. the pH of the medium. The voltammograms are recorded in 1.0 mM $\text{Na}_3[\text{Ru}_2(\mu\text{-CO}_3)_4]$ and 0.10 M NaHCO_3 aqueous solutions at different pHs with a scan rate of $50 \text{ mV}\cdot\text{s}^{-1}$ under N_2 atmosphere.

2.2.3. The Third Wave, $\text{Ru}^{\text{IV}}\text{Ru}^{\text{IV}}/\text{Ru}^{\text{IV}}\text{Ru}^{\text{III}}$ Redox Couple

The third peak is observed at 1.35 V and is due to a proton coupled one electron oxidation of $[\text{Ru}^{\text{IV}}\text{Ru}^{\text{III}}(\mu\text{-CO}_3)_4(\text{OH})(\text{CO}_3)]^{4-}$ to $[\text{Ru}^{\text{IV}}\text{Ru}^{\text{IV}}(\mu\text{-CO}_3)_4(\text{O})(\text{CO}_3)]^{4-}$ (Equation (23)). After the formation of $[\text{Ru}^{\text{IV}}\text{Ru}^{\text{IV}}(\mu\text{-CO}_3)_4(\text{O})(\text{CO}_3)]^{4-}$, the axial carbonate decomposes to form $[\text{Ru}^{\text{IV}}\text{Ru}^{\text{IV}}(\mu\text{-CO}_3)_4(\text{O})_2]^{4-}$ (Equation (24)). Equations (23) and (24) are based on the DFT calculations, see below.





Since the catalytic process starts at this stage, the current measured represents a process involving many electrons. The dependence of E_{pa} of the third process on the pH is plotted in Figure 9. The slope of the line in Figure 9 is $-84 \text{ mV} \cdot \text{pH}^{-1}$, thus pointing out that this is a PCET process.

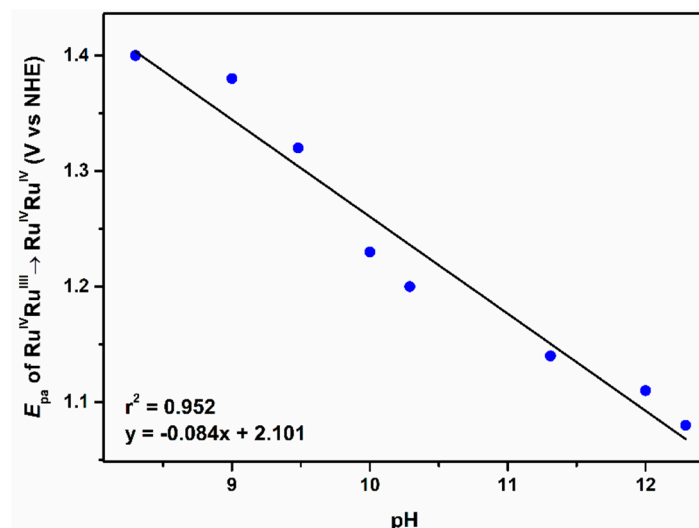
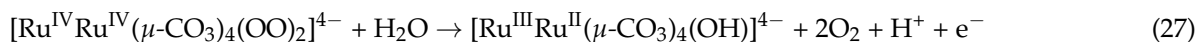


Figure 9. A plot of the anodic peak potential (E_{pa}) of the $\text{Ru}^{\text{IV}}\text{Ru}^{\text{IV}}/\text{Ru}^{\text{IV}}\text{Ru}^{\text{III}}$ redox couple vs. the pH of the medium. The voltammograms are recorded in 1.0 mM $\text{Na}_3[\text{Ru}_2(\mu\text{-CO}_3)_4]$ and 0.10 M NaHCO_3 aqueous solutions at different pHs with a scan rate of $50 \text{ mV} \cdot \text{s}^{-1}$ under N_2 atmosphere.

2.2.4. The Fourth Wave, Catalytic Oxidation

The catalytic oxidation of water/ HCO_3^- occurs at potentials $\geq 1.5 \text{ V}$ and proceeds via reactions (25)–(31) as derived by DFT, see below:

Two site mechanism:



Single site mechanism:



The catalytic process is homogeneous as the catalytic peak current increases linearly with the catalyst concentration (Figures 10 and S10).

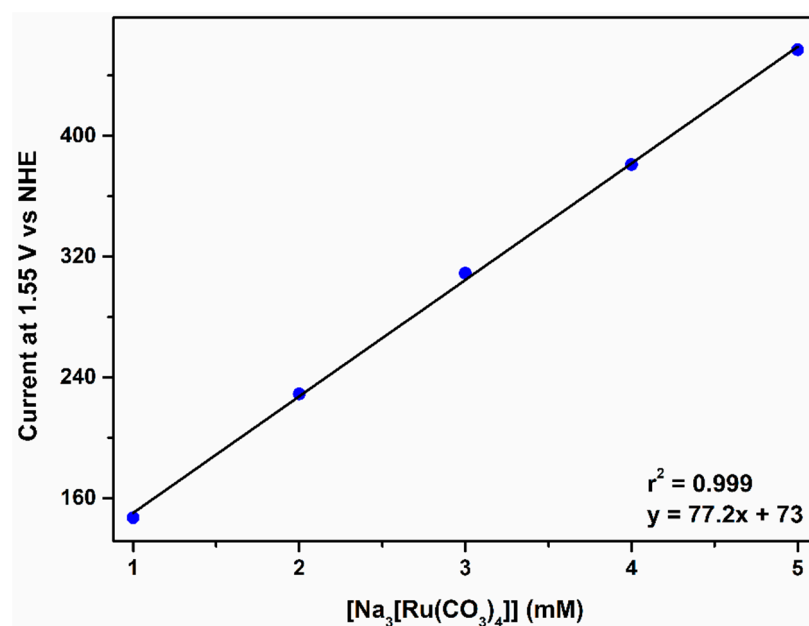


Figure 10. A linear increase of the catalytic peak current at 1.55 V vs. [Na₃[Ru₂(μ-CO₃)₄]]. The voltammograms are recorded in 0.10 M NaHCO₃ (pH 8.3) under N₂ atmosphere with a scan rate of 50 mV·s⁻¹.

The catalytic peak/plateau current also depends linearly on [HCO₃⁻] (Figures 11 and S11).

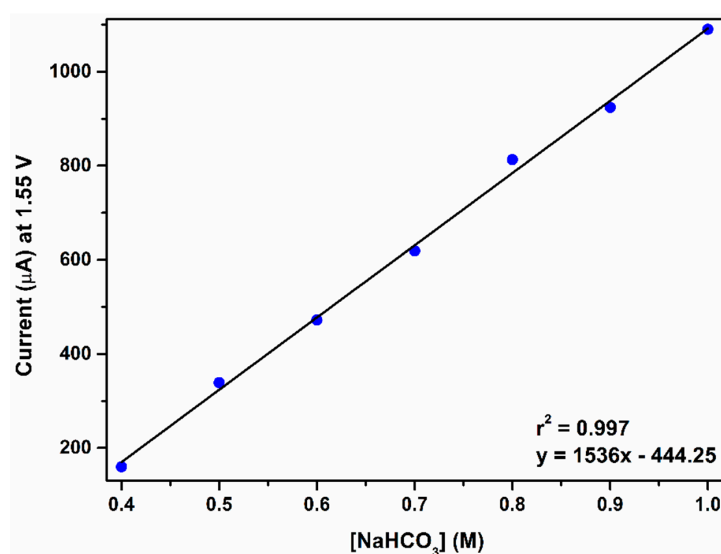


Figure 11. A plot of the catalytic peak/plateau current at 1.55 V vs. [NaHCO₃]. The voltammograms are recorded in 1.0 mM Na₃[Ru₂(μ-CO₃)₄] with increasing concentrations of NaHCO₃ (pH 8.3) at a scan rate of 50 mV·s⁻¹.

Involvement of protons in the catalytic process is demonstrated from the cathodic shift of the onset peak potential (E_{po}) with the increase in pH with a slope of $-48 \text{ mV}\cdot\text{pH}^{-1}$ (Figures 12 and S12). Discussing the first oxidation step in the presence of bicarbonate, it was suggested that after one electron oxidation, the species formed is $[\text{Ru}^{\text{III}}\text{Ru}^{\text{III}}(\mu\text{-CO}_3)_4(\text{OH})_2]^{4-}$ (Equation (22)). The redox behavior in the region 0 to 1.1 to -0.9 V (Figure S13) was studied where in the reverse scan three reduction peaks at 0.40, 0.10, and -0.55 V vs. NHE are observed due to the following processes (Equations (32)–(34)). On the other hand, in the same solution, when an identical scan is performed in the region 0 to -0.9 V , only one prominent reversible reduction peak is observed at -0.75 V vs. NHE (Figure S14)

that is due to the reduction of $[\text{Ru}^{\text{III}}\text{Ru}^{\text{II}}(\mu\text{-CO}_3)_4(\text{OH})]^{4-}$ to $[\text{Ru}^{\text{II}}\text{Ru}^{\text{II}}(\mu\text{-CO}_3)_4]^{6-}$. The other peaks are not observed, hence when the scan is first performed up to 1.1 V, then the first hydroxide gets coordinated on the oxidized species and the reduction peaks of various species can be seen. It is important to note that all the processes observed are diffusion controlled and no heterogeneous processes are taking place (Figures S15–S17). The last reduction peak is further studied (Figure S18) and the diffusion coefficient, D_R is found to be $2.64 \times 10^{-6} \text{ cm}^2 \cdot \text{s}^{-1}$ and the rate constant of electron transfer, k_0 to be $(3.12 \pm 0.30) \times 10^{-3} \text{ cm s}^{-1}$ (Table S2).

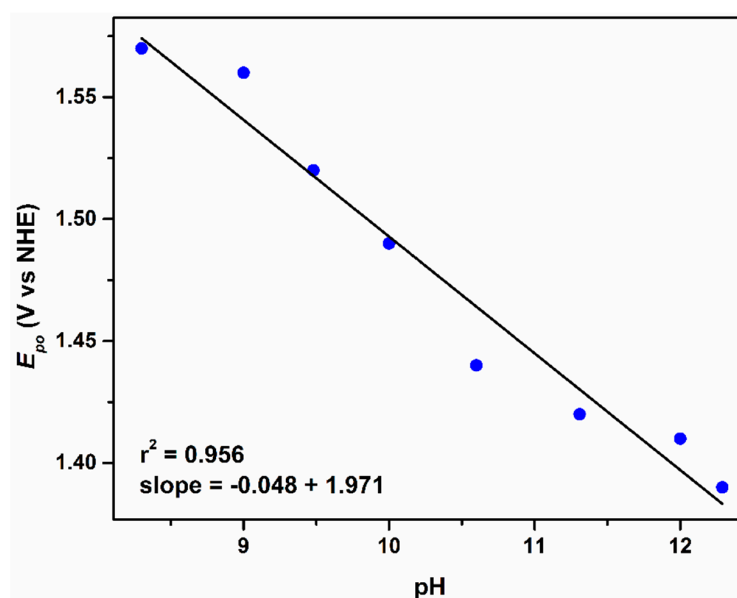


Figure 12. Variation of the catalytic water oxidation potential with pH. The voltammograms are recorded in solutions containing 1.0 mM $\text{Na}_3[\text{Ru}_2(\mu\text{-CO}_3)_4]$ in 0.10 M NaHCO_3 at various pHs under N_2 atmosphere, scan rate $50 \text{ mV} \cdot \text{s}^{-1}$. The onset potential is taken at a current of $400 \mu\text{A}$.

In the absorption spectra of the $[\text{Ru}^{\text{III}}\text{Ru}^{\text{II}}(\mu\text{-CO}_3)_4]^{3-}$ complex, two peaks are observed at $\lambda = 337 \text{ nm}$ ($\epsilon = 336 \text{ dm}^3 \cdot \text{mol}^{-1} \cdot \text{cm}^{-1}$) and 412 nm ($\epsilon = 834 \text{ dm}^3 \cdot \text{mol}^{-1} \cdot \text{cm}^{-1}$) (Figure S19). The first peak is due to the transition from the b_{2g} to the b_{1u} orbital, i.e., $\delta_{\text{Ru-Ru}} \rightarrow \delta_{\text{Ru-Ru}}^*$ and the second one is attributed to the transition from b_{2g} to a_{1g} and a_{2u} , i.e., $\delta_{\text{Ru-Ru}} \rightarrow \sigma_n / \sigma'_n$ [62]. For better understanding of the electronic transitions, a molecular orbital picture of the metal-metal bonding is given in Figure S20 [60,62]. A very weak signal is observed at $\approx 700 \text{ nm}$ due to the ligand to metal (Ru^{III}) charge transfer transition (MLCT) [63]. However, when the spectrum is recorded in bicarbonate media, no spectral changes are observed. Thus bicarbonate/carbonates are not bound to the axial position of the Ru atoms in this medium. Further, to check the stability of the complex, WOC long term chronoamperometry was performed at 1.6 V to follow the change in the current. Interestingly, the current does not change/decrease even after 15 h of chronoamperometry (Figure S21). However, in the electronic spectrum, the intensity of the peak at 708 nm is increased (Figure S22) after the chronoamperometry. This is because both the metals are present in a higher oxidation state. Moreover, this peak at 708 nm can also be observed after adding H_2O_2 to a solution of the complex in bicarbonate medium (Figure S23). This indicates the formation of $\text{Ru}=\text{O}$ species [64]. Further, activity has been checked by recording 250 voltametric scans successively, and no change in the current was

observed (Figure S24). The homogeneous nature of the catalysis has been confirmed by taking scanning electron microscope images before and after the chronoamperometry; no significant precipitate formation on the electrode surface has been observed (Figure S25), and in the energy dispersive X-ray analysis (EDAX), no Ru content has been found.

The Tafel plot obtained by plotting the overpotential (η) vs. $\log(\text{current density})$ (Figure S26) gives a slope of $229 \text{ mV} \cdot \text{dec}^{-1}$. For water oxidation catalysis, this usually falls in the range $40\text{--}200 \text{ mV} \cdot \text{dec}^{-1}$ [65], and with the heterogeneous catalysts, NiCo_2O_4 –nanosheets [66], the maximum value of $393 \text{ mV} \cdot \text{dec}^{-1}$ has also been reported. A large value of the Tafel slope means that the rate determining step is neither electrochemical nor chemical and is affected by the experimental conditions [67].

Some researcher describe this fact as the involvement of non-homogeneity and local defects due to bubble formation [68,69]. However, in neutral solutions containing no bicarbonate, the Tafel slope is $185 \text{ mV} \cdot \text{dec}^{-1}$ (Figure S27). The current of an electrocatalytic process is given by Equation (35), where n_c is the number of electrons involved in the catalytic process, the area A of the electrode in cm^2 , $[C]$ is the bulk concentration of the oxidized species in $\text{mol} \cdot \text{cm}^{-3}$, D_O is the diffusion coefficient of the oxidized species in $\text{cm}^2 \cdot \text{s}^{-1}$, k_{cat} is the catalytic rate constant in s^{-1} , and F is Faraday constant. Thus, in an electrocatalytic process, the catalytic current (i_c) is independent of the scan rate [70–74]. The relation of i_c/i_d with the inverse of the square root of the scan rate (Equation (36)) is obtained by dividing the Randles-Sevcik equation (Equation (20)) by Equation (35).

$$i_c = n_c F A [C] (k_{\text{cat}} D_{\text{Co}})^{\frac{1}{2}} \quad (35)$$

$$\frac{i_c}{i_d} = 0.359 \frac{n_{\text{cat}}}{n_d^{3/2}} \sqrt{\frac{k_{\text{cat}}}{\alpha v}} \quad (36)$$

where n_d is the number of electrons involved in the diffusion-controlled process, which is 3 here for the $\text{Ru}^{\text{IV}}\text{Ru}^{\text{IV}}/\text{Ru}^{\text{III}}\text{Ru}^{\text{II}}$ couple. The scan rate dependent voltammograms are given in Figure S28. The catalytic rate constant, $k_{\text{cat}} = 1.48 \text{ s}^{-1}$, is obtained from the slope of the plot of i_c/i_d vs. $v^{-1/2}$ (Figure 13). When the catalysis in neutral medium is considered, the value is 0.10 s^{-1} (Figures S29 and S30). Closely related values of 1.00 and 2.23 s^{-1} have been reported by Liobet and co-workers in out/in- $[\text{Ru}(\text{HL})(\text{trpy})(\text{H}_2\text{O})]^{2+}$ (HL = 1H-pyrazole-3-carboxylic acid, 5-(2-pyridinyl)-, ethyl ester). However, there are reports of the ruthenium complex, $[\text{Ru}(\text{bda})(\text{isoq})_2]$ ($\text{H}_2\text{bda} = 2,2'$ -bipyridine-6,6'-dicarboxylic acid; isoq = isoquinoline) [75] where the k_{cat} is 300 s^{-1} .

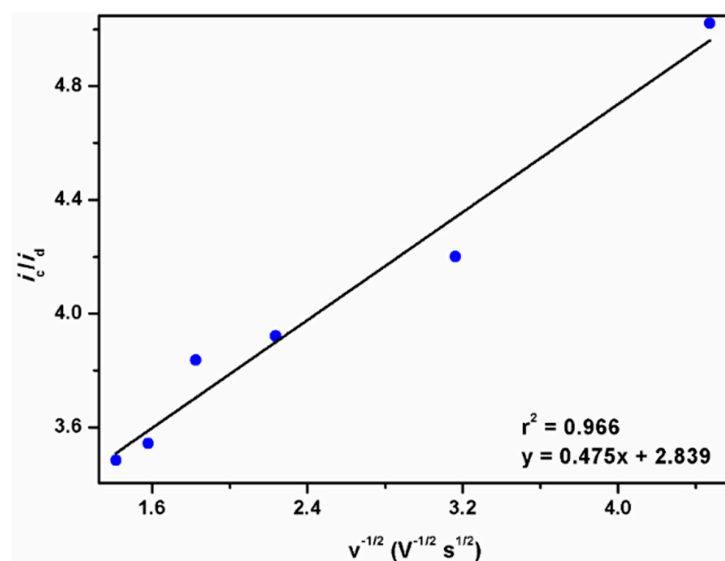


Figure 13. A plot of i_c/i_d vs. $v^{-1/2}$ for a solution containing $1.0 \text{ mM Na}_3[\text{Ru}_2(\mu\text{-CO}_3)_4]$ in 0.10 M NaHCO_3 ($\text{pH} = 8.3$). The i_c is taken at 1.56 V .

2.3. Theoretical Analysis of the Mechanism

To track the water oxidation route in the presence of the rigid bimetallic ruthenium $[\text{Ru}^{\text{III}}\text{Ru}^{\text{II}}(\mu\text{-CO}_3)_4]^{3-}$ (I_0) complex and to better understand the plausible nature of the intermediates formed in situ, DFT analysis was performed.

The plausible intermediates formed during the WOC process are schematically shown in Figure 14, and the relevant geometrical parameters are collected in Table 1. In order to validate the reliability of the computational level, the calculation was initiated following the optimization of the complex $[\text{Ru}^{\text{III}}\text{Ru}^{\text{II}}(\mu\text{-CO}_3)_4]^{3-}$ (I_0). Notably, the computed structural features correspond well to the experimental geometric data and support an electronic quartet ground state [59]. Initially, I_0 promptly reacts with water to form -OH coordinated I_1 species. The high exothermicity (-102.32 kcal/mol) drives the reaction forward. By moving from $\text{I}_0 \rightarrow \text{I}_1$, the Ru–Ru bond is slightly elongated, and the positive partial charges at the Ru centers are reduced (Table 1). The relatively less positive partial charge at the Ru^{III} ($\rho_{\text{Ru}1} = 0.762$ e) center compared to Ru^{II} ($\rho_{\text{Ru}1} = 0.968$ e) is attributed to the charge transfer from the OH^- ligand, coordinated to the Ru^{III} . The next step involves a proton-coupled electron transfer (PCET) event to generate I_2 , that is associated with the simultaneous change in the formal oxidation state from $\text{Ru}^{\text{II}} \rightarrow \text{Ru}^{\text{III}}$. This process comprises a favorable energy change of -17.17 kcal/mol. In I_2 , the two Ru^{III} centers have an almost equal charge ($\rho_{\text{Ru}1/\text{Ru}2} = 0.960/0.923$ e) and -OHs are ligated symmetrically with the ruthenium centers ($\text{Ru}1\text{-O}1 = 2.087$ Å and $\text{Ru}2\text{-O}2 = 2.038$ Å, Table 1). HCO_3^- participates in the next reaction and coordinates as CO_3^{2-} to the Ru^{IV} center by replacing the OH^- ligand with the simultaneous release of a proton and electron. The formation of I_3 from I_2 is a slightly uphill process ($\Delta G^0 = 3.88$ kcal/mol, Figure 14) and is easily accessible when the potential is applied. The one-electron oxidation of I_3 is coupled with the release of a proton from the OH^- ligand, leading to the formation of a $\text{Ru}^{\text{IV}}=\text{O}$ species I_4 (Figure 14). In I_4 , the charge discrepancies of the two Ru^{IV} centers are due to different extent of charge transfer of the coordinating oxo and CO_3^{2-} ligands ($\rho_{\text{Ru}1/\text{Ru}2} = 1.752/1.969$ e). Thereafter, two possible reaction channels can contribute, originating from I_4 . A single site mechanism, where water is involved in the percarbonate formation reaction and Ru^{IV} is reduced to Ru^{II} (I_5). This finally releases O_2 through an exergonic process to re-evolve complex I_1 for the next cycle. It is important to note that the partial charges between two Ru^{IV} centers in I_8 ($\rho_{\text{Ru}1/\text{Ru}2} = 1.002/1.002$ e) and I_{10} ($\rho_{\text{Ru}1/\text{Ru}2} = 0.788/0.785$ e) are symmetrically distributed. The slightly different charge distribution between two Ru^{III} centers is, however, noticed in I_9 ($\rho_{\text{Ru}1/\text{Ru}2} = 0.394/0.462$ e), can be explained by comparing the asymmetrical coordination of the -OOH ligands with the ruthenium centers ($\text{Ru}1\text{-O}1 = 2.043$ Å vs. $\text{Ru}2\text{-O}2 = 2.135$ Å, Table 1).

Comparing the two different potential pathways, it is clear that the transformation of $\text{I}_4 \rightarrow \text{I}_5$ associated with percarbonate formation is more exothermic ($\Delta G^0 = -111.51$ kcal/mol) than the alternative CO_2 dissociation process (i.e., $\text{I}_4 \rightarrow \text{I}_8$, $\Delta G^0 = -0.61$ kcal/mol), which directs the reaction to follow the single-site mechanism. Moreover, frontier molecular orbital analysis of I_5 shows that the lowest unoccupied molecular orbital (α -LUMO) has a significant contribution of the $\text{Ru}^{\text{IV}}=\text{O}$ π^* interaction, in which the weights of the p(O) and $d_{xz}(\text{Ru})$ atomic orbitals are 64% and 23%, respectively (Figure 15). A similar orbital interaction is also noticed for I_8 . The atomic orbital contributions correspond to the $\text{Ru}^{\text{IV}}=\text{O}$ π^* interaction is lower in I_8 (p(O) = 10% and $d_{xz}(\text{Ru}) = 36\%$), indicating a relatively lower propensity towards nucleophilic water attack [72]. These results agree with previous theoretical findings that a single ruthenium center is mainly involved in the water oxidation process [69].

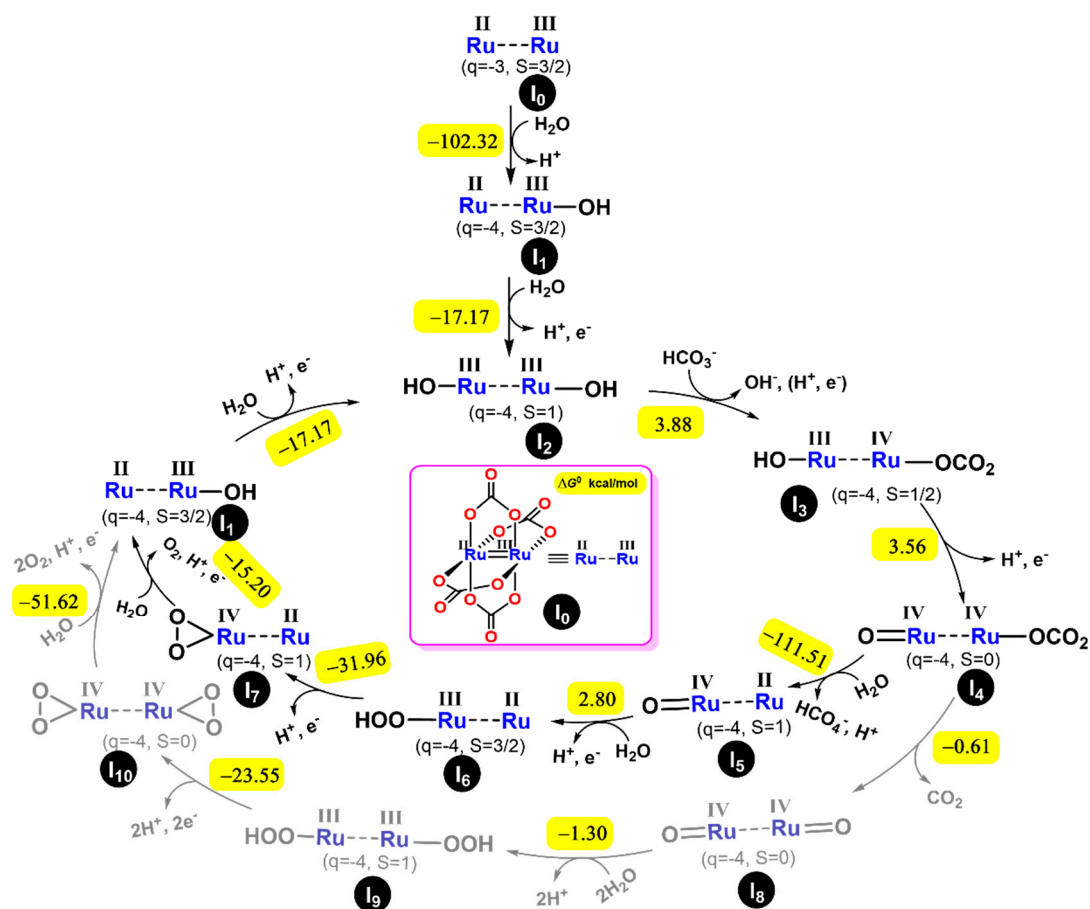


Figure 14. Schematic mechanism of the electrocatalytic water oxidation in the presence of $[Ru^{III}Ru^{II}(\mu-CO_3)_4]^{3-}$ (I_0). The free energies of the reactions are highlighted in yellow (ΔG° , kcal/mol). The grey part represents the double site mechanism and the black one the single site mechanism.

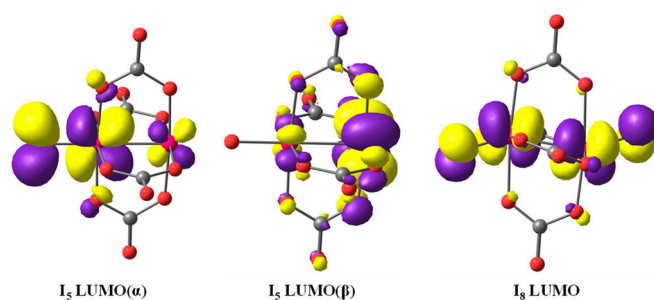


Figure 15. LUMO representations for the species $[Ru^{IV}Ru^{II}(\mu-CO_3)_4(O)]^{4-}$ (I_5) and $[Ru^{IV}Ru^{IV}(\mu-CO_3)_4(O)_2]^{4-}$ (I_8).

Moreover, to simulate the experimentally observed ultraviolet-visible (UV-Vis) spectra, we performed time dependent DFT (TD-DFT) calculations. Our results calculated $[Ru^{III}Ru^{III}(\mu-CO_3)_4(OH)_2]^{4-}$ (I_1) species revealed a characteristic peak at 426.9 nm that closely approximates the experimentally observed peak at 412 nm.

Table 1. Electronic and structural data for species involved in the water oxidation catalysts (WOC) mechanism.

Species	Configuration	Spin	q ^a	d ^b _{Ru1-Ru2}	d ^c _{Ru1-O1/Ru2-O2}	ρ ^d _{Ru1/Ru2}
I ₀	Ru ^{II} -Ru ^{III} d ⁶ -d ⁵	3/2	−3	2.235(2.260) ^e	-	1.052/1.074
I ₁	Ru ^{II} -Ru ^{III} d ⁶ -d ⁵	3/2	−4	2.334	-/2.070	0.968/0.762
I ₂	Ru ^{III} -Ru ^{III} d ⁵ -d ⁵	1	−4	2.318	2.087/2.038	0.960/0.923
I ₃	Ru ^{III} -Ru ^{IV} d ⁵ -d ⁴	1/2	−4	2.458	2.059/1.928	1.160/1.058
I ₄	Ru ^{IV} -Ru ^{IV} d ⁴ -d ⁴	0	−4	2.458	1.752/1.969	1.084/0.991
I ₅	Ru ^{IV} -Ru ^{II} d ⁴ -d ⁶	1	−4	2.422	1.850/-	0.839/1.027
I ₆	Ru ^{III} -Ru ^{II} d ⁵ -d ⁶	3/2	−4	2.303	2.023/-	0.712/0.979
I ₇	Ru ^{IV} -Ru ^{II} d ⁴ -d ⁶	1	−4	2.347	2.094/-	0.731/1.128
I ₈	Ru ^{IV} -Ru ^{IV} d ⁴ -d ⁴	0	−4	2.444	1.769/1.769	1.002/1.002
I ₉	Ru ^{III} -Ru ^{III} d ⁵ -d ⁵	1	−4	2.342	2.043/2.135	0.394/0.462
I ₁₀	Ru ^{IV} -Ru ^{IV} d ⁴ -d ⁴	0	−4	2.523	2.080/2.080	0.788/0.785

^a Overall system charge. ^b Ru^I-Ru² bond distances in Å. ^c Ruthenium-oxygen (ligands coordinating during WOC process). ^d Partial natural bond orbital (NBO) charges. ^e Value in parenthesis correspond to X-ray bond distance.

3. Materials and Methods

The Synthesis of Na₃[Ru₂(μ-CO₃)₄], details of the materials used and their sources, the instrumental specification, measurements, and the pretreatment/polishing of the glassy-carbon (GC) electrode (ALS the electrochemical company, Tokyo, Japan) are outlined in the Supplementary Material. The methods for the calculation of diffusion coefficients and electron transfer rate constants are also given in the Supplementary Material.

3.1. Electrochemistry Methods

The electrochemical results were obtained with an EmStat³ instrument (PalmSens, Compact Electrochemical Interfaces, Randhoeve 221, 3995 GA Houten, The Netherlands). The experiments were carried out using a three-electrode setup; glassy-carbon working electrode, diameter 3.0 mm, Ag/AgCl reference electrode, and a Pt counter electrode under N₂ atmosphere. Three electrochemical methods: Cyclic voltammetry, square wave voltammetry, and chrono-amperometry were used. All potentials given in this paper, if not specifically stated, are vs. normal hydrogen electrode (NHE) using the conversion: $E_{\text{NHE}} = E_{\text{Ag/AgCl}} + 0.198$.

3.2. Computational Details

A hybrid functional, Becke's three-parameter Lee-Yang-Parr (B3LYP) [76,77], was used for geometry optimization using the density functional theory (DFT) method implemented in the Gaussian16 [78] quantum chemistry software (C.01). The Pople's basis set 6-311+G(d,p) is utilized for all the non-metal atoms, whereas the well-established Stuttgart/Dresden (SDD) basis set with the effective core potential (ECP) was exploited for Ru. In addition, the dispersion effect was imposed using the Grimme D3 correction [79] with Becke-Johnson damping (BJ) during geometry minimization. The vibration frequency

analyses were performed at the same theoretical level to ensure the real minima ($N_{\text{img}} = 0$) and to obtain the thermodynamic energy corrections. The hydration effect was considered by a self-consistent reaction field (SCRf) approach using Truhler's SMD model [80] with default parameters for water. In solution, most of the species were defined by 1 (M) standard state, and 55.5 (M) was considered for water. Therefore, for other concentrations (C), additional corrections were made according to the following equation: $RT\ln(C)$. The exact calculation of a proton free energy in solution is not straight forward, and thus, we adopted a value of $-272.20 \text{ kcal mol}^{-1}$. Natural bond orbital (NBO) analysis implemented in Gaussian16 is used to calculate partial charges and Wiberg indices, which are a measure of bond orders. In order to compare the excitation energies obtained from the experimental UV-vis spectra, TD-DFT calculation was performed utilizing long-range corrected hybrid CAM-B3LYP functional [81]. The 3D images of the optimized structures were captured using CYLview20 visualization software. Unless explicitly stated, all reported energies are the Gibbs free energies in kcal mol^{-1} .

4. Conclusions

The results point out that $\text{Na}_3[\text{Ru}^{\text{III}}\text{Ru}^{\text{II}}(\mu\text{-CO}_3)_4]$ acts as an efficient water oxidation catalyst in neutral medium and in the presence of bicarbonate/carbonate. In neutral solutions, the first oxidation peak can be seen, but the other intermediate oxidation steps are not seen before the electrocatalytic water oxidation step. On the other hand, in the bicarbonate medium before water oxidation the formation of other intermediate species are observed in cyclic voltammetry. It is found that all the electrochemical processes involved are proton coupled electron transfers (PCET). The catalytic peak/plateau current depends linearly on the catalyst and on the bicarbonate concentrations. Thus, it is clear that bicarbonate is involved in the process of oxidation. Furthermore, after the formation of $[\text{Ru}^{\text{IV}}\text{Ru}^{\text{III}}(\mu\text{-CO}_3)_4(\text{OH})(\text{CO}_3)]^{2-}$ by three electron oxidations when the reverse scan is performed, all the other steps can be seen in the presence of bicarbonate, which cannot be observed in the absence of bicarbonate. This catalyst has the advantage that it contains no organic ligand and is therefore stable during the catalytic cycles.

Supplementary Materials: The following are available online at <https://www.mdpi.com/2073-4344/11/2/281/s1>. Table S1: The values of anodic peak (E_{pa} (V)) and cathodic (E_{pc} (V)) peak potential, their difference, ΔE_{p} (V); Nicholson parameter, ψ and rate constant of electron transfer, k_0 (cm s^{-1}) at different scan rate (V s^{-1}) for the redox couple $\text{Ru}^{\text{III}}\text{Ru}^{\text{III}}/\text{Ru}^{\text{III}}\text{Ru}^{\text{II}}$ in neutral medium, Table S2: The values of E_{pa} (V), E_{pc} (V), ΔE_{p} (V), ψ and k_0 (cm s^{-1}) at different scan rate (V s^{-1}) for the redox couple $\text{Ru}^{\text{IV}}\text{Ru}^{\text{V}}/\text{Ru}^{\text{IV}}\text{Ru}^{\text{IV}}$ in bicarbonate medium, Table S3: The values of E_{pa} (V), E_{pc} (V), ΔE_{p} (V), ψ and k_0 (cm s^{-1}) at different scan rate (V s^{-1}) for the redox couple for the redox couple $\text{Ru}^{\text{II}}\text{Ru}^{\text{III}}/\text{Ru}^{\text{II}}\text{Ru}^{\text{II}}$ in bicarbonate medium, Figure S1: The crystal structure of $\text{Na}_3[\text{Ru}(\mu\text{-CO}_3)_4]$ showing the axial coordination of carbonate ligand from another complex. CCDC No. 1200939, Figure S2: CVs of 1.0 mM $\text{Na}_3[\text{Ru}_2(\mu\text{-CO}_3)_4]$ in 0.20 M NaClO_4 (pH 7.0) and 1 mM $\text{K}_4[\text{Fe}(\text{CN})_6]$ and 0.20 M NaClO_4 at a scan rate of $50 \text{ mV}\cdot\text{s}^{-1}$, Figure S3: CVs of 1.0 mM $\text{Na}_3[\text{Ru}_2(\mu\text{-CO}_3)_4]$ in 0.20 M NaClO_4 (pH 7.0) at various scan rates, Figure S4: CVs of 1.0 mM $\text{Na}_3[\text{Ru}_2(\mu\text{-CO}_3)_4]$ in 0.20 M NaClO_4 solution at different pHs with a scan rate of $50 \text{ mV}\cdot\text{s}^{-1}$ highlighting the first redox couple, Figure S5: CVs of 1.0 mM $\text{Na}_3[\text{Ru}_2(\mu\text{-CO}_3)_4]$ in 0.20 M NaClO_4 solution at different pHs with a scan rate of $50 \text{ mV}\cdot\text{s}^{-1}$, Figure S6: CVs of 1.0 mM $\text{Na}_3[\text{Ru}_2(\mu\text{-CO}_3)_4]$ and 1.0 mM $\text{K}_4[\text{Fe}(\text{CN})_6]$ in 0.10 M NaHCO_3 (pH 8.3) at a scan rate of $50 \text{ mV}\cdot\text{s}^{-1}$, Figure S7: CVs of 1.0 mM $\text{Na}_3[\text{Ru}_2(\mu\text{-CO}_3)_4]$ in 0.10 M NaHCO_3 solution at different pHs with a scan rate of $50 \text{ mV}\cdot\text{s}^{-1}$, Figure S8: CVs of 1.0 mM $\text{Na}_3[\text{Ru}_2(\mu\text{-CO}_3)_4]$ in 0.10 M NaHCO_3 (pH 8.3) at various scan rates highlighting the first two redox processes, Figure S9: CVs of increasing concentrations of NaHCO_3 (pH 8.3) in 1.0 mM $\text{Na}_3[\text{Ru}_2(\mu\text{-CO}_3)_4]$ with a scan rate of $50 \text{ mV}\cdot\text{s}^{-1}$ highlighting the $\text{Ru}^{\text{III}}\text{Ru}^{\text{III}}/\text{Ru}^{\text{III}}\text{Ru}^{\text{II}}$ redox couple, Figure S10: CVs of increasing concentrations of $\text{Na}_3[\text{Ru}_2(\mu\text{-CO}_3)_4]$ in 0.10 M NaHCO_3 (pH 8.3) with a scan rate of $50 \text{ mV}\cdot\text{s}^{-1}$, Figure S11: CVs of increasing concentrations of NaHCO_3 (pH 8.3) in 1.0 mM $\text{Na}_3[\text{Ru}_2(\mu\text{-CO}_3)_4]$ with a scan rate of $50 \text{ mV}\cdot\text{s}^{-1}$, Figure S12: The CVs of 1.0 mM $\text{Na}_3[\text{Ru}_2(\mu\text{-CO}_3)_4]$ in 0.19 M NaHCO_3 at various pHs with a scan rate of $50 \text{ mV}\cdot\text{s}^{-1}$, Figure S13: CVs of 1.0 mM $\text{Na}_3[\text{Ru}_2(\mu\text{-CO}_3)_4]$ in 0.10 M NaHCO_3 (pH 8.3) at various scan rates, Figure S14: CVs of 1.0 mM $\text{Na}_3[\text{Ru}_2(\mu\text{-CO}_3)_4]$ in 0.10 M NaHCO_3 (pH 8.3) at various scan rates, Figure S15: i_{d} at E_{pc} of 0.11 V vs. $v^{1/2}$ in 1.0 mM

$\text{Na}_3[\text{Ru}_2(\mu\text{-CO}_3)_4]$ and 0.10 M NaHCO_3 (pH 8.3), Figure S16: i_d at E_{pc} of -0.50 V vs. $v^{1/2}$ in 1.0 mM $\text{Na}_3[\text{Ru}_2(\mu\text{-CO}_3)_4]$ and 0.10 M NaHCO_3 (pH 8.3), Figure S17: i_d at E_{pc} of -0.75 V vs. $v^{1/2}$ in 1.0 mM $\text{Na}_3[\text{Ru}_2(\mu\text{-CO}_3)_4]$ and 0.10 M NaHCO_3 (pH 8.3), Figure S18: CVs of 5.0 mM $\text{Na}_3[\text{Ru}_2(\mu\text{-CO}_3)_4]$ in 0.10 M NaHCO_3 (pH 8.3) highlighting the $\text{Ru}^{\text{III}}\text{Ru}^{\text{II}}/\text{Ru}^{\text{II}}\text{Ru}^{\text{II}}$ couple, Figure S19: Absorption spectra of 1.0 mM $\text{Na}_3[\text{Ru}_2(\mu\text{-CO}_3)_4]$ in presence and absence of 0.10 M NaHCO_3 , Figure S20: A qualitative MO diagram of the metal-metal bonding for an M_2X_8 (M = transition metal and X is halide) species of symmetry D_{4h} . The electron distribution shown is that for $[\text{Ru}_2(\mu\text{-CO}_3)_4]^{3+}$, Figure S21: The chronoamperometry (CA) of 1.0 mM $\text{Na}_3[\text{Ru}_2(\mu\text{-CO}_3)_4]$ in 0.10 M NaHCO_3 at pH 8.3 for 15 h at a potential of 1.6 V vs. NHE, Figure S22: Absorption spectra before and after chronoamperometry of a solution containing 1.0 mM $\text{Na}_3[\text{Ru}_2(\mu\text{-CO}_3)_4]$, 0.10 M NaHCO_3 at 1.6 V vs. NHE for 15 h, Figure S23: Comparison of the electronic absorption spectra of 1.0 mM $\text{Na}_3[\text{Ru}_2(\mu\text{-CO}_3)_4]$, 0.10 M NaHCO_3 in presence and absence of NaHCO_3 , Figure S24: The SEM image of the GC electrode before and after chronoamperometry, Figure S25: Successive CVs of 1.0 mM $\text{Na}_3[\text{Ru}_2(\mu\text{-CO}_3)_4]$ in 0.10 M NaHCO_3 (pH 8.3) at a scan rate of 50 mV s^{-1} , Figure S26: Tafel plot in presence of bicarbonate. LSV is recorded in 1.0 mM $\text{Na}_3[\text{Ru}_2(\mu\text{-CO}_3)_4]$ in 0.10 M NaHCO_3 at pH 8.3 at a scan rate of 50 mV s^{-1} , Figure S27: Tafel plot under neutral condition. LSV is recorded in a solution containing 1.0 mM $\text{Na}_3[\text{Ru}_2(\mu\text{-CO}_3)_4]$ in 0.20 M NaClO_4 at pH 7.0 at a scan rate of 50 mV s^{-1} , Figure S28: CVs of 1.0 mM $\text{Na}_3[\text{Ru}_2(\mu\text{-CO}_3)_4]$ in 0.10 M NaHCO_3 at pH 8.3 at various scan rates, Figure S29: CVs of 1.0 mM $\text{Na}_3[\text{Ru}_2(\mu\text{-CO}_3)_4]$ in 0.20 M NaClO_4 at pH 7.0 at various scan rates, Figure S30: A Plot of i_c/i_d vs. $v^{-1/2}$ for a solution containing 1.0 mM $\text{Na}_3[\text{Ru}_2(\mu\text{-CO}_3)_4]$ in 0.20 M NaClO_4 (pH 7.0). The i_c is taken at 1.56 V.

Author Contributions: Conceptualization, S.G.P. and D.M.; methodology, S.G.P., T.M., K.S., D.M., H.K., and A.M.; software, H.K.; validation, S.G.P., D.M., and H.K.; investigation, S.G.P., T.M., K.S., D.M., H.K., and A.M.; resources, D.M.; writing—original draft preparation, S.G.P. and D.M.; writing—review and editing, S.G.P., D.M., T.M., H.K., A.M.; visualization, S.G.P. and T.M.; supervision, D.M. and H.K.; project administration, D.M.; funding acquisition, D.M., and A.M. All authors have read and agreed to the published version of the manuscript.

Funding: This research was funded by PAZY FOUNDATION, grant number RA 1700000337.

Data Availability Statement: Data available on request. Some data can also be found in the Supplementary Material.

Acknowledgments: We are indebted to the Pazy foundation for financial support that enabled this study. SGP thanks Ariel University and Dan Meyerstein for post-doctoral fellowship.

Conflicts of Interest: The authors declare no conflict of interest

References

1. Shatskiy, A.; Kärkäs, M.D.; Åkermark, B. The Art of Splitting Water: Storing Energy in a Readily Available and Convenient Form. *Eur. J. Inorg. Chem.* **2019**, 2019, 2020–2024. [[CrossRef](#)]
2. Dresselhaus, M.S.; Thomas, I.L. Alternative energy technologies. *Nature* **2001**, *414*, 332–337. [[CrossRef](#)] [[PubMed](#)]
3. Ort, D.R.; Yocum, C.F.; Heichel, I.F. (Eds.) Oxygenic photosynthesis: The light reactions. In *Advances in Photosynthesis and Respiration*; Springer: Dordrecht, The Netherlands, 1996; Volume 4, ISBN 978-0-7923-3683-9.
4. Meyer, T.J.; Huynh, M.H.V.; Thorp, H.H. The possible role of proton-coupled electron transfer (PCET) in water oxidation by photosystem II. *Angew. Chemie Int. Ed.* **2007**, *46*, 5284–5304. [[CrossRef](#)] [[PubMed](#)]
5. Xu, Y.; Kraft, M.; Xu, R. Metal-free carbonaceous electrocatalysts and photocatalysts for water splitting. *Chem. Soc. Rev.* **2016**, *45*, 3039–3052. [[CrossRef](#)]
6. Tian, T.; Zheng, M.; Lin, J.; Meng, X.; Ding, Y. Amorphous Ni-Fe double hydroxide hollow nanocubes enriched with oxygen vacancies as efficient electrocatalytic water oxidation catalysts. *Chem. Commun.* **2019**, *55*, 1044–1047. [[CrossRef](#)] [[PubMed](#)]
7. Fukuzumi, S.; Lee, Y.M.; Nam, W. Kinetics and mechanisms of catalytic water oxidation. *Dalt. Trans.* **2019**, *48*, 779–798. [[CrossRef](#)]
8. Lee, Y.; Suntivich, J.; May, K.J.; Perry, E.E.; Shao-Horn, Y. Synthesis and Activities of Rutile IrO_2 and RuO_2 Nanoparticles for Oxygen Evolution in Acid and Alkaline Solutions. *J. Phys. Chem. Lett.* **2012**, *3*, 399–404. [[CrossRef](#)] [[PubMed](#)]
9. Peng, L.; Shah, S.S.A.; Wei, Z. Recent developments in metal phosphide and sulfide electrocatalysts for oxygen evolution reaction. *Chin. J. Catal.* **2018**, *39*, 1575–1593. [[CrossRef](#)]
10. Hunter, B.M.; Gray, H.B.; Müller, A.M. Earth-Abundant Heterogeneous Water Oxidation Catalysts. *Chem. Rev.* **2016**, *116*, 14120–14136. [[CrossRef](#)] [[PubMed](#)]
11. Wasylenko, D.J.; Palmer, R.D.; Berlinguette, C.P. Homogeneous water oxidation catalysts containing a single metal site. *Chem. Commun.* **2013**, *49*, 218–227. [[CrossRef](#)]

12. Parent, A.R.; Sakai, K. Progress in base-metal water oxidation catalysis. *ChemSusChem* **2014**, *7*, 2070–2080. [[CrossRef](#)]
13. Indra, A.; Menezes, P.W.; Driess, M. Uncovering structure-activity relationships in manganese-oxide-based heterogeneous catalysts for efficient water oxidation. *ChemSusChem* **2015**, *8*, 776–785. [[CrossRef](#)] [[PubMed](#)]
14. Liu, T.; Zhang, B.; Sun, L. Iron-Based Molecular Water Oxidation Catalysts: Abundant, Cheap, and Promising. *Chem. Asian J.* **2019**, *14*, 31–43. [[CrossRef](#)]
15. Kärkäs, M.D.; Åkermark, B. Water oxidation using earth-abundant transition metal catalysts: Opportunities and challenges. *Dalt. Trans.* **2016**, *45*, 14421–14461. [[CrossRef](#)]
16. Singh, A.; Spiccia, L. Water oxidation catalysts based on abundant 1st row transition metals. *Coord. Chem. Rev.* **2013**, *257*, 2607. [[CrossRef](#)]
17. Risch, M.; Klingan, K.; Zaharieva, I.; Dau, H. Water Oxidation by Co-Based Oxides with Molecular Properties. *Mol. Water Oxid. Catal. Key Top. New Sustain. Energy Convers. Schemes* **2014**, 9781118413, 163–185. [[CrossRef](#)]
18. Van Oversteeg, C.H.M.; Doan, H.Q.; De Groot, F.M.F.; Cuk, T. In situ X-ray absorption spectroscopy of transition metal based water oxidation catalysts. *Chem. Soc. Rev.* **2017**, *46*, 102–125. [[CrossRef](#)] [[PubMed](#)]
19. Basu, O.; Mukhopadhyay, S.; Das, S.K. Cobalt based functional inorganic materials: Electrocatalytic water oxidation. *J. Chem. Sci.* **2018**, *130*, 1–15. [[CrossRef](#)]
20. Patra, S.G.; Illés, E.; Mizrahi, A.; Meyerstein, D. Cobalt Carbonate as an Electrocatalyst for Water Oxidation. *Chem. A Eur. J.* **2020**, *26*, 711–720. [[CrossRef](#)] [[PubMed](#)]
21. Wang, J.W.; Liu, W.J.; Zhong, D.C.; Lu, T.B. Nickel complexes as molecular catalysts for water splitting and CO₂ reduction. *Coord. Chem. Rev.* **2019**, *378*, 237–261. [[CrossRef](#)]
22. Ariela, B.; Yaniv, W.; Dror, S.; Haya, K.; Yael, A.; Eric, M.; Dan, M. The role of carbonate in electro-catalytic water oxidation by using Ni(1,4,8,11-tetraazacyclotetradecane) 2+. *Dalt. Trans.* **2017**, *46*, 10774–10779. [[CrossRef](#)] [[PubMed](#)]
23. Liu, S.; Lei, Y.J.; Xin, Z.J.; Lu, Y.B.; Wang, H.Y. Water splitting based on homogeneous copper molecular catalysts. *J. Photochem. Photobiol. A Chem.* **2018**, *355*, 141–151. [[CrossRef](#)]
24. Shaffer, D.W.; Xie, Y.; Concepcion, J.J. O-O bond formation in ruthenium-catalyzed water oxidation: Single-site nucleophilic attack: Vs. O-O radical coupling. *Chem. Soc. Rev.* **2017**, *46*, 6170–6193. [[CrossRef](#)] [[PubMed](#)]
25. Corbucci, I.; Macchioni, A.; Albrecht, M. Iridium Complexes in Water Oxidation Catalysis. *Iridium(III) Optoelectron. Photonics Appl.* **2017**, 617–654. [[CrossRef](#)]
26. Matheu, R.; Ertem, M.Z.; Gimbert-Suriñach, C.; Sala, X.; Llobet, A. Seven Coordinated Molecular Ruthenium-Water Oxidation Catalysts: A Coordination Chemistry Journey. *Chem. Rev.* **2019**, *119*, 3453–3471. [[CrossRef](#)]
27. Blakemore, J.D.; Crabtree, R.H.; Brudvig, G.W. Molecular Catalysts for Water Oxidation. *Chem. Rev.* **2015**, *115*, 12974–13005. [[CrossRef](#)] [[PubMed](#)]
28. Gersten, S.W.; Samuels, G.J.; Meyer, T.J. Catalytic oxidation of water by an oxo-bridged ruthenium dimer. *J. Am. Chem. Soc.* **1982**, *104*, 4029–4030. [[CrossRef](#)]
29. Zhang, B.; Sun, L. Artificial photosynthesis: Opportunities and challenges of molecular catalysts. *Chem. Soc. Rev.* **2019**, *48*, 2216–2264. [[CrossRef](#)] [[PubMed](#)]
30. Stull, J.A.; Stich, T.A.; Hurst, J.K.; Britt, R.D. Electron paramagnetic resonance analysis of a transient species formed during water oxidation catalyzed by the complex ion [(bpy)₂Ru(OH₂)₂O⁴⁺]. *Inorg. Chem.* **2013**, *52*, 4578–4586. [[CrossRef](#)]
31. Yamada, H.; Siems, W.F.; Koike, T.; Hurst, J.K. Mechanisms of water oxidation catalyzed by the cis,cis-[(bpy)₂Ru(OH₂)₂O⁴⁺ ion. *J. Am. Chem. Soc.* **2004**, *126*, 9786–9795. [[CrossRef](#)]
32. Moonshiram, D.; Jurss, J.W.; Concepcion, J.J.; Zakharova, T.; Alperovich, I.; Meyer, T.J.; Pushkar, Y. Structure and electronic configurations of the intermediates of water oxidation in blue ruthenium dimer catalysis. *J. Am. Chem. Soc.* **2012**, *134*, 4625–4636. [[CrossRef](#)] [[PubMed](#)]
33. Yamada, H.; Hurst, J.K. Resonance raman, optical spectroscopic, and EPR characterization of the higher oxidation states of the water oxidation catalyst, cis,cis-[(bpy)₂Ru(OH₂)₂O⁴⁺]. *J. Am. Chem. Soc.* **2000**, *122*, 5303–5311. [[CrossRef](#)]
34. Moonshiram, D.; Alperovich, I.; Concepcion, J.J.; Meyer, T.J.; Pushkar, Y. Experimental demonstration of radicaloid character in a Ru^V=O intermediate in catalytic water oxidation. *Proc. Natl. Acad. Sci. USA* **2013**, *110*, 3765–3770. [[CrossRef](#)]
35. Cape, J.L.; Hurst, J.K. Detection and mechanistic relevance of transient ligand radicals formed during [Ru(bpy)₂(OH₂)₂O⁴⁺-catalyzed water oxidation. *J. Am. Chem. Soc.* **2008**, *130*, 827–829. [[CrossRef](#)]
36. Najafpour, M.M.; Renger, G.; Hołyńska, M.; Moghaddam, A.N.; Aro, E.M.; Carpentier, R.; Nishihara, H.; Eaton-Rye, J.J.; Shen, J.R.; Allakhverdiev, S.I. Manganese Compounds as Water-Oxidizing Catalysts: From the Natural Water-Oxidizing Complex to Nanosized Manganese Oxide Structures. *Chem. Rev.* **2016**, *116*, 2886–2936. [[CrossRef](#)] [[PubMed](#)]
37. Moyer, B.A.; Meyer, T.J. Properties of the oxo/aqua system (bpy)₂(py)RuO₂⁺/(bpy)₂(py)Ru(OH₂)₂⁺. *Inorg. Chem.* **1981**, *20*, 436–444. [[CrossRef](#)]
38. Moyer, B.A.; Meyer, T.J. Oxobis(2,2'-bipyridine)pyridineruthenium(IV) ion, [(bpy)₂(py)Ru:O]²⁺. *J. Am. Chem. Soc.* **1978**, *100*, 3601–3603. [[CrossRef](#)]
39. Tong, L.; Thummel, R.P. Mononuclear ruthenium polypyridine complexes that catalyze water oxidation. *Chem. Sci.* **2016**, *7*, 6591–6603. [[CrossRef](#)] [[PubMed](#)]
40. Gagliardi, C.J.; Vannucci, A.K.; Concepcion, J.J.; Chen, Z.; Meyer, T.J. The role of proton coupled electron transfer in water oxidation. *Energy Environ. Sci.* **2012**, *5*, 7704. [[CrossRef](#)]

41. Jenson, D.L.; Barry, B.A. Proton-coupled electron transfer in photosystem II: Proton inventory of a redox active tyrosine. *J. Am. Chem. Soc.* **2009**, *131*, 10567–10573. [[CrossRef](#)]
42. Mizrahi, A.; Meyerstein, D. Plausible roles of carbonate in catalytic water oxidation. In *Advances in Inorganic Chemistry*; Elsevier: Amsterdam, The Netherlands, 2019; pp. 343–360.
43. Patra, S.G.; Mizrahi, A.; Meyerstein, D. The Role of Carbonate in Catalytic Oxidations. *Acc. Chem. Res.* **2020**, *53*, 2189–2200. [[CrossRef](#)]
44. Steenzen, S.; Neta, P.; Stanbury, D.M.; Armstrong, D.A.; Ruscic, B.; Koppenol, W.H.; Huie, R.E.; Merényi, G.; Wardman, P.; Lymar, S.V. Standard electrode potentials involving radicals in aqueous solution: Inorganic radicals (IUPAC Technical Report). *Pure Appl. Chem.* **2015**, *87*, 1139–1150. [[CrossRef](#)]
45. Zilberg, S.; Mizrahi, A.; Meyerstein, D.; Kornweitz, H. Carbonate and carbonate anion radicals in aqueous solutions exist as $\text{CO}_3(\text{H}_2\text{O})_6^{2-}$ and $\text{CO}_3(\text{H}_2\text{O})_6^-$ respectively: The crucial role of the inner hydration sphere of anions in explaining their properties. *Phys. Chem. Chem. Phys.* **2018**, *20*, 9429–9435. [[CrossRef](#)] [[PubMed](#)]
46. Wang, J.; Ji, L.; Chen, Z. In Situ Rapid Formation of a Nickel–Iron-Based Electrocatalyst for Water Oxidation. *ACS Catal.* **2016**, *6*, 6987–6992. [[CrossRef](#)]
47. Khorobrykh, A.; Dasgupta, J.; Kolling, D.R.J.; Terentyev, V.; Klimov, V.V.; Dismukes, G.C. Evolutionary Origins of the Photosynthetic Water Oxidation Cluster: Bicarbonate Permits Mn^{2+} Photo-oxidation by Anoxygenic Bacterial Reaction Centers. *ChemBioChem* **2013**, *14*, 1725–1731. [[CrossRef](#)]
48. Hobart, D.E.; Samhoun, K.; Young, J.P.; Norvell, V.E.; Mamantov, G.; Peterson, J.R. Stabilization of praseodymium(IV) and terbium(IV) in aqueous carbonate solution. *Inorg. Nucl. Chem. Lett.* **1980**, *16*, 321–328. [[CrossRef](#)]
49. Koroidov, S.; Shevela, D.; Shutova, T.; Samuelsson, G.; Messinger, J. Mobile hydrogen carbonate acts as proton acceptor in photosynthetic water oxidation. *Proc. Natl. Acad. Sci. USA* **2014**, *111*, 6299–6304. [[CrossRef](#)]
50. Shevela, D.; Nöring, B.; Koroidov, S.; Shutova, T.; Samuelsson, G.; Messinger, J. Efficiency of photosynthetic water oxidation at ambient and depleted levels of inorganic carbon. *Photosynth. Res.* **2013**, *117*, 401–412. [[CrossRef](#)]
51. Chen, Z.; Meyer, T.J. Copper(II) Catalysis of Water Oxidation. *Angew. Chemie Int. Ed.* **2013**, *52*, 700–703. [[CrossRef](#)]
52. Winikoff, S.G.; Cramer, C.J. Mechanistic analysis of water oxidation catalyzed by mononuclear copper in aqueous bicarbonate solutions. *Catal. Sci. Technol.* **2014**, *4*, 2484–2489. [[CrossRef](#)]
53. Mizrahi, A.; Maimon, E.; Cohen, H.; Kornweitz, H.; Zilbermann, I.; Meyerstein, D. Mechanistic Studies on the Role of $[\text{Cu}^{\text{II}}(\text{CO}_3)_n]^{2-2n}$ as a Water Oxidation Catalyst: Carbonate as a Non-Innocent Ligand. *Chem. A Eur. J.* **2018**, *24*, 1088–1096. [[CrossRef](#)]
54. Chen, F.; Wang, N.; Lei, H.; Guo, D.; Liu, H.; Zhang, Z.; Zhang, W.; Lai, W.; Cao, R. Electrocatalytic Water Oxidation by a Water-Soluble Copper(II) Complex with a Copper-Bound Carbonate Group Acting as a Potential Proton Shuttle. *Inorg. Chem.* **2017**, *56*, 13368–13375. [[CrossRef](#)]
55. Kuttassery, F.; Sebastian, A.; Mathew, S.; Tachibana, H.; Inoue, H. Promotive Effect of Bicarbonate Ion on Two-Electron Water Oxidation to Form H_2O_2 Catalyzed by Aluminum Porphyrins. *ChemSusChem* **2019**, *12*, 1939–1948. [[CrossRef](#)]
56. Haygarth, K.S.; Marin, T.W.; Janik, I.; Kanjana, K.; Stanisky, C.M.; Bartels, D.M. Carbonate radical formation in radiolysis of sodium carbonate and bicarbonate solutions up to 250 °C and the mechanism of its second order decay. *J. Phys. Chem. A* **2010**, *114*, 2142–2150. [[CrossRef](#)]
57. Lindsay, A.J.; Wilkinson, G.; Motevalli, M.; Hursthouse, M.B. Reactions of tetra- μ -carboxylato-diruthenium(II,II) compounds. X-Ray crystal structures of $\text{Ru}_2(\mu\text{-O}_2\text{CCF}_3)_4(\text{thf})_2$, $\text{Ru}_2(\mu\text{-O}_2\text{CR})_4$. *J. Chem. Soc. Dalton Trans.* **1987**, 2723–2736. [[CrossRef](#)]
58. Lindsay, A.J.; Motevalli, M.; Hursthouse, M.B.; Wilkinson, G. The synthesis and structure of the unusual polymeric compound $\{\text{Na}_3[\text{Ru}_2(\mu\text{-O}_2\text{CO})_4] \cdot 6\text{H}_2\text{O}\}_n$. *J. Chem. Soc. Chem. Commun.* **1986**, 2, 433–434. [[CrossRef](#)]
59. Cotton, F.A.; Labella, L.; Shang, M. Further study of tetracarboxylato diruthenium(II,III) compounds. *Inorg. Chem.* **1992**, *31*, 2385–2389. [[CrossRef](#)]
60. Cotton, F.A.; Murillo, C.A.; Walton, R.A. *Multiple Bonds between Metal Atoms*; Cotton, F.A., Murillo, C.A., Walton, R.A., Eds.; Springer: New York, NY, USA, 2005; ISBN 0-387-25084-0.
61. Nicholson, R.S. Theory and Application of Cyclic Voltammetry for Measurement of Electrode Reaction Kinetics. *Anal. Chem.* **1965**, *37*, 1351–1355. [[CrossRef](#)]
62. Bennett, M.J.; Caulton, K.G.; Cotton, F.A. Structure of tetra-*n*-butyratodiruthenium chloride, a compound with a strong metal-metal bond. *Inorg. Chem.* **1969**, *8*, 1–6. [[CrossRef](#)]
63. Guadalupe Hernández, J.; Huerta-Aguilar, C.A.; Thangarasu, P.; Höpfl, H. A ruthenium(III) complex derived from *N,N'*-bis(salicylidene)ethylenediamine as a chemosensor for the selective recognition of acetate and its interaction with cells for bio-imaging: Experimental and theoretical studies. *New J. Chem.* **2017**, *41*, 10815–10827. [[CrossRef](#)]
64. Wada, T.; Nishimura, S.; Mochizuki, T.; Ando, T.; Miyazato, Y. Mechanism of Water Oxidation Catalyzed by a Dinuclear Ruthenium Complex Bridged by Anthraquinone. *Catalysts* **2017**, *7*, 56. [[CrossRef](#)]
65. Bockris, J.O. The Electrocatalysis of Oxygen Evolution on Perovskites. *J. Electrochem. Soc.* **1984**, *131*, 290. [[CrossRef](#)]
66. Shi, H.; Zhao, G. Water Oxidation on Spinel NiCo_2O_4 Nanoneedles Anode: Microstructures, Specific Surface Character, and the Enhanced Electrocatalytic Performance. *J. Phys. Chem. C* **2014**, *118*, 25939–25946. [[CrossRef](#)]
67. Goberna-Ferrón, S.; Peña, B.; Soriano-López, J.; Carbó, J.J.; Zhao, H.; Poblet, J.M.; Dunbar, K.R.; Galán-Mascarós, J.R. A fast metal–metal bonded water oxidation catalyst. *J. Catal.* **2014**, *315*, 25–32. [[CrossRef](#)]

68. Blakemore, J.D.; Schley, N.D.; Olack, G.W.; Incarvito, C.D.; Brudvig, G.W.; Crabtree, R.H. Anodic deposition of a robust iridium-based water-oxidation catalyst from organometallic precursors. *Chem. Sci.* **2011**, *2*, 94–98. [[CrossRef](#)]
69. Schley, N.D.; Blakemore, J.D.; Subbaiyan, N.K.; Incarvito, C.D.; D'Souza, F.; Crabtree, R.H.; Brudvig, G.W. Distinguishing Homogeneous from Heterogeneous Catalysis in Electrode-Driven Water Oxidation with Molecular Iridium Complexes. *J. Am. Chem. Soc.* **2011**, *133*, 10473–10481. [[CrossRef](#)]
70. Wang, D.; Groves, J.T. Efficient water oxidation catalyzed by homogeneous cationic cobalt porphyrins with critical roles for the buffer base. *Proc. Natl. Acad. Sci. USA* **2013**, *110*, 15579–15584. [[CrossRef](#)]
71. Vannucci, A.K.; Meyer, T.J.; Dares, C.J.; Coggins, M.K.; Zhang, M.-T. Electrocatalytic Water Oxidation by a Monomeric Amidate-Ligated Fe(III)–Aqua Complex. *J. Am. Chem. Soc.* **2014**, *136*, 5531–5534. [[CrossRef](#)]
72. Koepke, S.J.; Light, K.M.; Vannatta, P.E.; Wiley, K.M.; Kieber-Emmons, M.T. Electrocatalytic Water Oxidation by a Homogeneous Copper Catalyst Disfavors Single-Site Mechanisms. *J. Am. Chem. Soc.* **2017**, *139*, 8586–8600. [[CrossRef](#)]
73. Wang, D.; Bruner, C.O. Catalytic Water Oxidation by a Bio-inspired Nickel Complex with a Redox-Active Ligand. *Inorg. Chem.* **2017**, *56*, 13638–13641. [[CrossRef](#)]
74. Du, H.Y.; Chen, S.C.; Su, X.J.; Jiao, L.; Zhang, M.T. Redox-Active Ligand Assisted Multielectron Catalysis: A Case of Co^{III} Complex as Water Oxidation Catalyst. *J. Am. Chem. Soc.* **2018**, *140*, 1557–1565. [[CrossRef](#)]
75. Duan, L.; Bozoglian, F.; Mandal, S.; Stewart, B.; Privalov, T.; Llobet, A.; Sun, L. A molecular ruthenium catalyst with water-oxidation activity comparable to that of photosystem II. *Nat. Chem.* **2012**, *4*, 418–423. [[CrossRef](#)]
76. Becke, A.D. Density-functional exchange-energy approximation with correct asymptotic behavior. *Phys. Rev. A* **1988**, *38*, 3098–3100. [[CrossRef](#)]
77. Lee, C.; Yang, W.; Parr, R.G. Development of the Colle-Salvetti correlation-energy formula into a functional of the electron density. *Phys. Rev. B* **1988**, *37*, 785–789. [[CrossRef](#)]
78. Frisch, M.J.; Trucks, G.W.; Schlegel, H.B.; Scuseria, G.E.; Robb, M.A.; Cheeseman, J.R.; Scalmani, G.; Barone, V.; Petersson, G.A.; Nakatsuji, H.; et al. *Gaussian 16, Revision C.01*; Gaussian, Inc.: Wallingford, CT, USA, 2016.
79. Grimme, S.; Antony, J.; Ehrlich, S.; Krieg, H. A consistent and accurate ab initio parametrization of density functional dispersion correction (DFT-D) for the 94 elements H–Pu. *J. Chem. Phys.* **2010**, *132*, 154104. [[CrossRef](#)] [[PubMed](#)]
80. Marenich, A.V.; Cramer, C.J.; Truhlar, D.G. Universal Solvation Model Based on Solute Electron Density and on a Continuum Model of the Solvent Defined by the Bulk Dielectric Constant and Atomic Surface Tensions. *J. Phys. Chem. B* **2009**, *113*, 6378–6396. [[CrossRef](#)] [[PubMed](#)]
81. Yanai, T.; Tew, D.P.; Handy, N.C. A new hybrid exchange–correlation functional using the Coulomb-attenuating method (CAM-B3LYP). *Chem. Phys. Lett.* **2004**, *393*, 51–57. [[CrossRef](#)]